Received: 24 November 2022 | Revised: 21 December 2023 | Accepted: 11 January 2024

DOI: 10.1002/esp.5778

RESEARCH ARTICLE

ESPL WILEY

Complex erosional response to uplift and rock strength contrasts in transient river systems crossing an active normal fault revealed by ^{10}Be and ^{26}Al cosmogenic nuclide analyses

Sarah J. Boulton[1] | Ángel Rodés[2] | Derek Fabel[2] | M. Cihat Alçiçek[3] | Alexander C. Whittaker[4]

[1]School of Geography, Earth and Environmental Sciences, University of Plymouth, Plymouth, UK

[2]Scottish Universities Environmental Research Centre, Glasgow, UK

[3]Department of Geological Engineering, Pamukkale University, Denizli, Türkiye

[4]Department of Earth Science and Engineering, Royal School of Mines, Imperial College, London, UK

Correspondence
Sarah J. Boulton, School of Geography, Earth and Environmental Sciences, University of Plymouth, Drake's Circus, Plymouth, PL4 8AA, UK.
Email: sarah.boulton@plymouth.ac.uk

Present address
Ángel Rodés, Departamento de Xeografía, Universidade de Santiago de Compostela, A Coruña, Spain.

Funding information
Natural Environment Research Council, Grant/Award Number: CIAF/9189/1018; The Geological Society

Abstract

Understanding the influence of bedrock lithology on the catchment-averaged erosion rates of normal fault-bounded catchments and the effect that different bedrock erodibilties have on the evolution of transient fluvial geomorphology remain major challenges. To investigate this problem, we collected 18 samples for ^{10}Be and ^{26}Al cosmogenic nuclide analysis to determine catchment-averaged erosion rates along the well-constrained Gediz Fault system in western Türkiye, which is experiencing fault-driven river incision owing to a linkage event ~0.8 Ma and has weak rocks overlying strong rocks in the footwall. Combined with existing cosmogenic data, we show that the background rate of erosion of the pre-incision landscape can be constrained as <92 mMyr^{-1}, and erosion rates within the transient reach vary from 16 to 1330 mMyr^{-1}. Erosion rates weakly scale with unit stream power, steepness index and slip rate on the bounding fault, although erosion rates are an order of magnitude lower than slip rates. However, there are no clear relationships between erosion rate and relief or catchment slope. Bedrock strength is assessed using Schmidt hammer rebound and Selby Rock Mass Strength Assessments; despite a 30-fold difference in erodibility, there is no difference in the erosion rate between strong and weak rocks. We argue that, for the Gediz Graben, the strong lithological contrast affects the ability of the river to erode the bed, resulting in a complex erosional response to uplift along the graben boundary fault. Weak covariant trends between erosion rates and various topographic factors potentially result from incomplete sediment mixing or pre-existing topographic inheritance. These findings indicate that the erosional response to uplift along an active normal fault is a complex response to multiple drivers that vary spatially and temporally.

KEYWORDS
active faulting, cosmogenic nuclides, detachment-limited, rock strength, Turkey, Türkiye

1 | INTRODUCTION

The role of climate, tectonics and lithology on the evolution and form of bedrock (detachment-limited) streams is well known. The effect of tectonics, in particular the effect of variable uplift rates (i.e. Kirby & Whipple, 2012; Whittaker, 2012; Whittaker & Boulton, 2012; Wobus et al., 2006), and climate gradients (Adams et al., 2020; D'Arcy & Whittaker, 2014) on the rates and patterns of incision have been widely reported. Until recently, the role of lithology and rock strength have attracted less attention, and many studies have sought to remove or minimise this variable by choosing study areas with little rock variation (e.g. Miller, Baldwin, & Fitzgerald, 2012; Ortega, Wohl, &

Livers, 2013; Regalla et al., 2013; Snyder et al., 2000). However, landscape evolution modelling (Darling et al., 2020; Forte & Whipple, 2018; Forte, Yanites, & Whipple, 2016; Mitchell & Yanites, 2021; Perne et al., 2017) and field investigations at the landscape (Bernard et al., 2019; Zondervan, Stokes, et al., 2020) and catchment scale (Duvall, 2004; Gailleton et al., 2021; Kent et al., 2021; Peifer et al., 2020; Sklar & Dietrich, 2001; Whittaker et al., 2007) have increasingly investigated the importance of lithology on river incision and fluvial geomorphology. Yet, there are still uncertainties in how bedrock properties influence catchment scale erosion and how such characteristics can be effectively measured in the field.

Furthermore, while a number of studies have directly compared catchment-averaged erosion rates (CAERs) to bedrock channel properties (i.e. Abbühl et al., 2011; Bellin, Vanacker, & Kubik, 2014; Cyr et al., 2010; DiBiase et al., 2010; Harkins et al., 2007; Kober et al., 2015; Miller et al., 2013; Ouimet, Whipple, & Granger, 2009; Safran et al., 2005), relatively few studies have determined CAER along the strike of an active fault. For example, Densmore et al. (2009) studied two faults in the western USA, the 18 km long Sweetwater fault and the 130 km Wassuk fault. Along neither fault were CAER found to be proportional to uplift rates along the fault nor to various topographic measures of the footwall geomorphology. Densmore et al. (2009) attributed the uncoupling of erosion from fault displacement to the influence of inherited high relief topography and the widespread occurrence of mass wasting. In contrast, Rossi et al. (2017) reported 26 erosion rates along a normal fault system in Baja California demonstrating a positive trend between CAER with slope and channel steepness. Roda-Boluda et al. (2019) also showed a linear relationship between CAER and the footwall component of fault throw rate from 15 samples taken from a series of catchments crossing an active normal fault system in southern Italy. In all these studies, the footwalls of the studied faults are composed of metamorphic or igneous rocks with limited reported lithological variability at a regional scale.

This lithological homogeneity of existing research areas is significant, as the modelling of Forte, Yanites and Whipple (2016) suggests that the presence of lithological contacts, where rock strength changes from strong to weak, will profoundly influence the response rates of an incising river system. For example, their modelling suggests that when soft rocks overlie hard rocks (along a contact dipping at 20–35° downstream) the lithological contact becomes an important and persistent topographic feature in the landscape. Interestingly, although the geological boundary moves downstream over time, the model suggests that erosion rates above and below the boundary should diverge. The soft rocks downstream erode at the imposed uplift rate, but the underlying hard rocks erode at a rate lower than the regional uplift rate (Forte, Yanites, & Whipple, 2016). The difference in the strength and bedrock erodibility between the hard and soft rocks controls the magnitude of difference between erosion and uplift rate, and also the duration of the landscape adjustment. Subsequent modelling studies by Perne et al. (2017), Darling et al. (2020), Wolpert and Forte (2021) and Mitchell and Yanites (2021) are broadly consistent with Forte, Yanites and Whipple (2016)'s results. Although the more complex interbedded hard-soft rock scenarios of Darling et al. (2020)'s model indicate that in such cases the harder rocks may erode quicker than the soft rocks. A further implication of Forte et al.'s (Forte, Yanites, & Whipple, 2016) landscape evolution model is that CAER, determined from cosmogenic radionuclides (CRN, commonly ^{10}Be), may be affected by the relative enrichment of material from the harder rocks in the detrital sediment. Consequently, CAER would be perturbed or amplified because of the lithological variation.

Therefore, there is a knowledge gap in our understanding of how erosion rates change along faults with lithologically variable footwall geology. There is also the requirement to empirically test the results of models such as Forte, Yanites and Whipple (2016), Perne et al. (2017) and Darling et al. (2020) in regions with complex geology to assess the applicability of these models to real systems.

Here, we use the well-constrained Gediz fault system (western Türkiye) as a natural laboratory to study the landscape response to fluvial incision across a strong lithological contrast (soft rocks over hard rocks) in the footwall of an active normal fault. As the geologic and geomorphic evolution of the region is well understood and constrained (i.e. Bozkurt, 2003; Bozkurt & Sözbilir, 2004; Çiftçi & Bozkurt, 2009; Kent, 2015; Kent et al., 2017, Kent et al., 2021; Öner & Dilek, 2011; Seyitoğlu & Scott, 1996; Seyitoğlu et al., 2002), we can use the area to test the model predictions of Forte, Yanites and Whipple (2016) and investigate the role that strength contrasts play in the evolution of transient landscape responses to base-level fall. This is achieved through a suite of new ^{10}Be and ^{26}Al CRN samples to determine CAER along the strike of the boundary faults combined with published cosmogenic data (Buscher et al., 2013; Heineke et al., 2019) and geomorphic indices (Kent et al., 2021). CAERs are quantified using ^{10}Be and ^{26}Al so that the potential effect of sediment storage can be excluded, thus allowing accurate exposure and denudation histories to be calculated (c.f. Bierman et al., 1999; Granger & Muzikar, 2001; von Blanckenburg, 2006).

2 | STUDY AREA

The Gediz (also known as the Alaşehir) Graben is located in western Anatolia (Figure 1) forming an arcuate, asymmetric graben ~150 km in length. The Bozdağ Range to the south is uplifted along the southern graben-bounding normal fault and rises to over 2000 m in elevation. The approximate N-S extension forming this horst and graben structure has been ongoing since early Miocene times, probably as the result of roll-back along the Hellenic subduction zone (Okay & Satır, 2000; Ten Veen et al., 2009), and can be divided into two main phases (Bozkurt & Sözbilir, 2004). Initial extension caused uplift along the now-inactive low-angle north-dipping Gediz detachment fault (Gessner et al., 2001; Seyitoğlu et al., 2002; Ring et al., 2003). The Gediz detachment fault presently dips to the N-NE at up to 32° and is gently corrugated along its strike (Bozkurt & Sozbilir, 2004). The detachment forms the boundary between the Menderes Massif metamorphic rocks and overlying syn-tectonic sedimentary rocks (Figure 2). In the footwall, the Menderes Massif metamorphic core complex is composed mainly of Palaeozoic greenschist to amphibolite-facies schists, augengneisses and paragneisses (Gessner et al., 2001; Ring et al., 2003).

Following the cessation of slip on the Gediz detachment fault at ~2 Ma (Buscher et al., 2013), strain stepped northwards (basinwards) onto high angle faults. These include the presently active normal fault forming the range front fault (Figures 1 and 2) to the present-day

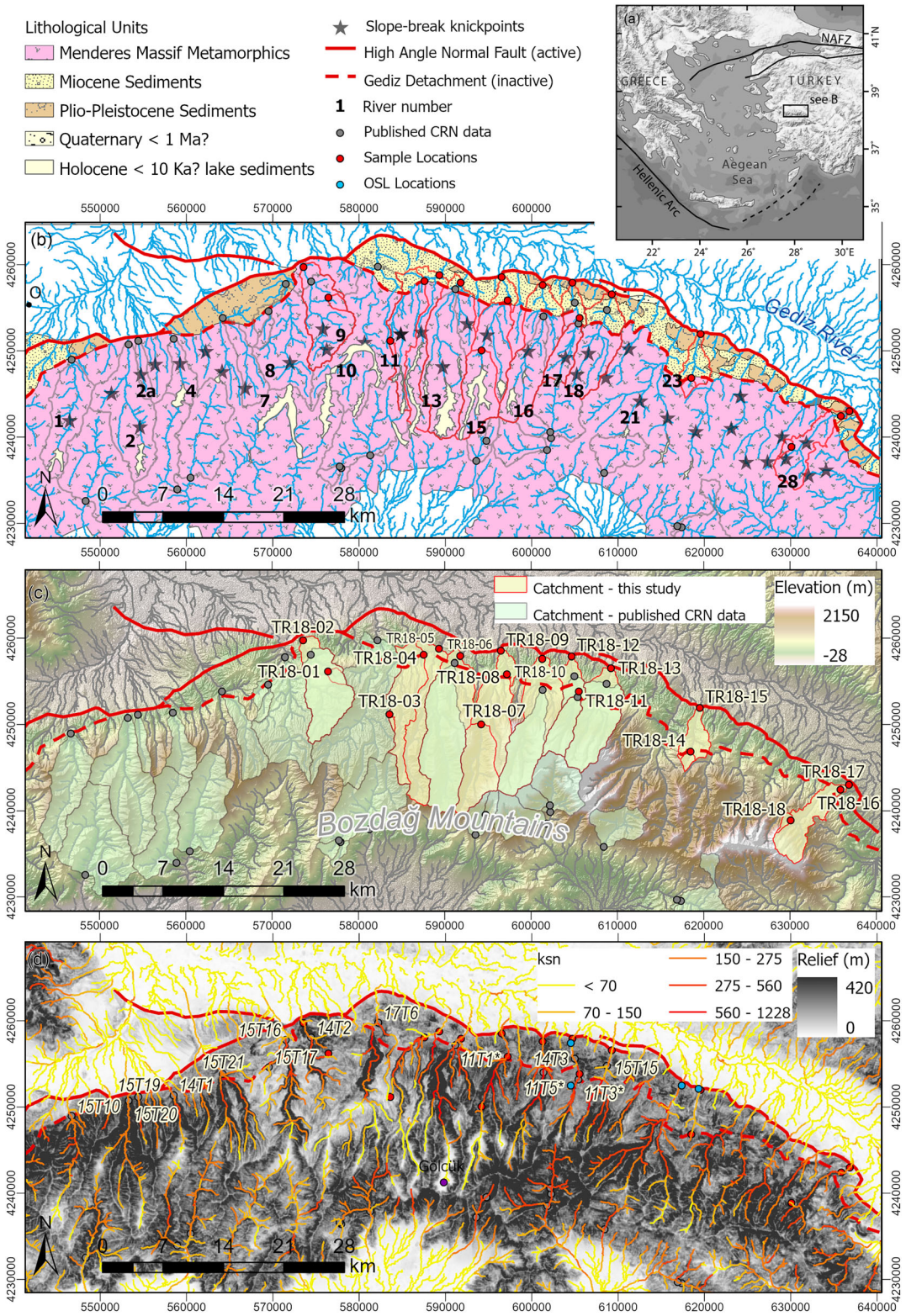

FIGURE 1 (a) Regional location map showing the location of the Gediz Graben in Western Anatolia; (b) Geological map of the study area. Geological units are simplified from Kent et al. (2021) with additional mapping of Holocene lake deposits from Süzen, Toprak and Rojay (2006). Numbers in bold indicate rivers sampled for cosmogenic radionuclides (CRN) either in this study (Table 1) or by Heineke et al. (2019) or Buscher et al. (2013) (Table 3), rivers mentioned by name in the text are 9, Akçapınar; 15, Bozdağ; 16, Gümüşcay; 17, Kabazli; 21, Kavaklidere; 23, Yeniköy. Stars show location of slope-break knickpoints; (c) topographic map of the study area (ALOS World 3D 30 m digital elevation model) showing the locations with numbers of samples collected during this study; (d) relief map of the study are showing the steepness index of the rivers and the location of CRN samples collected by Buscher et al. (2013) indicated by * and Heineke et al. (2019). Also shown are the location of five optically stimulated luminescence dates reported by Kent (2015) (unlabelled, blue circles) and the approximate location of the C^{14} date of Sullivan (1988) labelled as Gölcük. [Color figure can be viewed at wileyonlinelibrary.com]

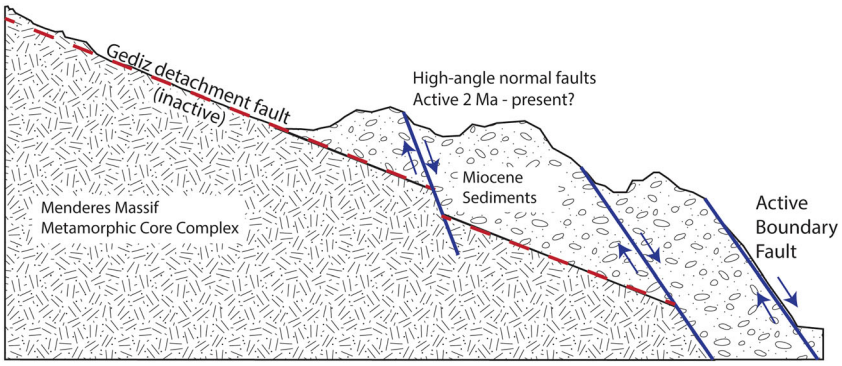

FIGURE 2 Simplified cross-section of the northern margin of the Bozdağ Horst showing the relationship between low and high-angle faults (adapted from Kent et al., 2016). [Color figure can be viewed at wileyonlinelibrary.com]

topographic graben (Çiftçi & Bozkurt, 2009). In the uplifted footwall of the active fault are friable sedimentary rocks deposited originally on the hanging wall of the Gediz detachment. These sedimentary units, comprised mainly of early Miocene to Pliocene-aged alluvial fan and fluvial sandstones and conglomerates, unconformably overlie and derive from the metamorphic basement (e.g. Çiftçi & Bozkurt, 2009; Purvis & Robertson, 2004, 2005).

Quaternary sediments are variable in extent across the Bozdağ range (Figure 1). Fragments of river terraces have been reported by Kent (2015) along three rivers—the Yeniköy, Kavaklıdere and the Kabazlı (Figure 1b). These river terraces are of small spatial extent with OSL dates of five samples (Figure 1d) from the fine-grained facies of only one, well-developed, terrace level indicating aggradation between ~84–7.5 ka (Kent, 2015). However, in the headwaters of several of the larger river systems, fluvial and lacustrine fine-grained sediments up to 170 m thick can be found (Süzen, Toprak, & Rojay, 2006). Sediment cores from Gölcük Lake (Figure 1d) yielded ^{14}C dates of ≤10 ka (Sullivan, 1988), suggesting deposition during the Holocene to Pleistocene, but ages of the older sediments are not constrained. These deposits are thought to have formed owing to 1–2° of rotation on the graben boundary fault during the Holocene resulting in slope reduction, lake formation and sediment deposition (Süzen, Toprak, & Rojay, 2006).

Across the Bozdağ Range, transverse bedrock rivers flow northwards into the Gediz Graben across the southern boundary fault. The rivers are generally deeply incised with prominent knickpoints and gorges upstream of the active fault. The slope-break knickpoints are not coincident with lithological boundaries (Kent et al., 2017) and are interpreted to mark the upstream extent of transient wave of river incision. Incision was caused by an increase in slip on the graben bounding fault as a result of the fault linkage of three initial fault segments ~0.6–1 Ma (Kent, 2015; Kent et al., 2017). As a result of this linkage, present day throw rates (the vertical component of the slip rate) are now thought to be higher than the long-term average, with rates of up to 2 ± 0.2 mmyr^{-1} calculated for the centre of the fault array (Kent et al., 2017).

Kent et al. (2021) selected six of the transverse rivers to investigate the lithological controls on transient river behaviour. For simplicity, Kent et al. (2021) used two broad groupings of rock types: metamorphic and sedimentary in their quantitative analyses. Rivers were chosen to investigate differences in the proportion of metamorphic to sedimentary bedrock reaches (100% metamorphic in the Akçapınar River through to ~50% along the Yeniköy River; Figure 1b) and differences in uplift rate as a result of activity along the graben boundary fault. Here, we continue to use these two broad lithologic groups to allow comparisons to this previous work.

3 | METHODS

3.1 | Sample collection and CRN

Eighteen samples of river sand from the active riverbed or sediment bars (Figures 1c and 3) were collected from nine catchments draining northwards across the Gediz Graben boundary fault in May 2018 (Figures 1c and S3). The rivers were selected because either they had previously been sampled by Buscher et al. (2013) or were one of the six rivers studied in detail by Kent et al. (2021). Overall, a nested sampling strategy was adopted so that 10 samples were collected from the range front where the rivers cross the active normal fault. On the easternmost river, two samples were collected ~2 km apart to assess downstream mixing and reproducibility. The remaining eight samples collected further upstream at either the lithological boundary between the sedimentary and metamorphic rocks or upstream of the knickpoint. Five of these eight samples were collected upstream of identified slope-break (tectonic) knickpoints identified by Kent et al. (2017), and the final three samples were collected at the low-angle detachment that forms the lithological boundary enabling comparison to published datasets. A further CRN dataset was published by Heineke et al. (2019) bringing the total number of samples analysed in the Gediz region to 33.

The 18 samples collected here were sieved to 2 mm in field and further sieved to the 250–500 μm size fraction in the lab. Standard magnetic separation to concentrate the quartz fraction of the sample using a Franz magnetic separator was undertaken at the University of Plymouth. Subsequently, samples were chemically leached using diluted HF, and between 16 and 20 g of clean quartz cores were dissolved at SUERC together with ~0.29 g of the CIAF-PH9 in-house ^{9}Be carrier solution ([Be] = 849 ± 12 ppm) following the procedure of Child et al. (2000). ^{10}Be and ^{26}Al concentrations were measured by the 5-MV NEC Pelletron accelerator mass spectrometer (AMS) at SUERC (Xu et al., 2010).

The results were input into the online CRONUS-Earth calculator v 3.0 (Balco et al., 2008) using the LSDn scaling, a sample density of 2.65 gcm^{3} and NIST_27900 and Z92-0222 standardisations for ^{10}Be and ^{26}Al, respectively. Mean catchment elevation and shielding were derived from the ALOS World3D 30 m DEM, which has been shown to extract more accurate hydrological networks than other

comparable global DEMs (Boulton & Stokes, 2018) using ArcGIS Pro 2.6.2 and TopoToolBox functions (Schwanghart & Scherler, 2014). Similarly, catchment mean slope and relief over a 150 m radius were extracted using standard GIS tools.

Burial ages were derived from ^{10}Be and ^{26}Al data following the same principles as Granger and Muzikar (2001). This method allows solving of both the erosion rate corresponding to the initial ^{10}Be and ^{26}Al concentrations, and the average burial time after the exhumation of the quartz grains. To make them consistent with CRONUS v.3 results, scaled concentrations, spallation and muon production rates, and attenuation lengths were calculated as in Rodés (2021).

We also recalculated the ^{10}Be sample concentrations reported in Buscher et al. (2013) and Heineke et al. (2019) for our study area using the same parameters stated above (e.g. using topographic shielding and a sample density of 2.65 gcm^3 and CRONUS v 3 (Table S1). Note that Heineke et al. (2019) did not apply a topographic shielding and used a sample density of 2.2–2.5 gcm^3 in addition to using v 2.3 of the CRONUS-Earth calculator, which results in differences in the erosion rates stated here compared to those reported in the original papers. Neither of these previous studies included ^{26}Al concentrations, so corrections for sediment reworking or burial cannot be determined for these previously published CRN data .

3.2 | Sediment (un)mixing

In the Bozdağ catchments, studied samples were taken at the catchment outlet, at the major lithological boundary and in five locations above the slope-break knickpoint. This sampling strategy allows the erosion rates above (un-incised) and below (incised) the slope-break knickpoint to be deconvolved assuming that the same amount of quartz-bearing sediment is produced in both parts of the watershed. The sediment mixing is determined using the approach of Granger, Kirchner and Finkel (1996), as the CRN records the average erosion rate for the entire contributing catchment area. Therefore, the erosion rate between two sample points (a 'subcatchment') can be determined by correcting for the upstream sediment flux according to

$$E_b = \frac{(E_c \times A_c) - (E_a \times A_a)}{A_b}, \quad (1)$$

where E (mMyr^{-1}) is the erosion rate of a catchment with area A (m^2), with subscripts indicting different subcatchments (Figure 4), where *c* is the entire catchment and *a* and *b* are the upstream and downstream subcatchments, respectively. In this study, a *single* common value for the upstream erosion rate E_A is used for all catchments owing to: (a) the limited data on the CAER above the knickpoint, (b) the assumption that this area represents a low relief and low erosion rate landscape formed prior to the uplift causing the present transient river incision.

ArcGIS Pro 2.6.2 was used to calculate the areas used in the unmixing calculations. The knickpoint finder tool in TopoToolBox (Schwanghart & Scherler, 2014; Stolle et al., 2019) was used to identify the highest knickpoint along all tributaries in the study area using a tolerance of 30. These were then used as pour points for the watershed tool, the results of which were then summed to determine the total unincised area in each river catchment, which is then subtracted from the total catchment area calculated in the same way for the sample locations.

FIGURE 3 Field photos showing landscapes and sampling in the Gediz region: (a) view of the downstream reach of the Akçapınar River—a river characterised by 100% metamorphic bedrock, (b) sampling in the knickzone of the Bozdağ River, (c) sampling in the sedimentary reach of the Gümüşçay (note the well lithified Miocene clastic bedrock), (d) vertical step knickzone on the Kabazlı River at the boundary between the metamorphic basement and the sedimentary cover. [Color figure can be viewed at wileyonlinelibrary.com]

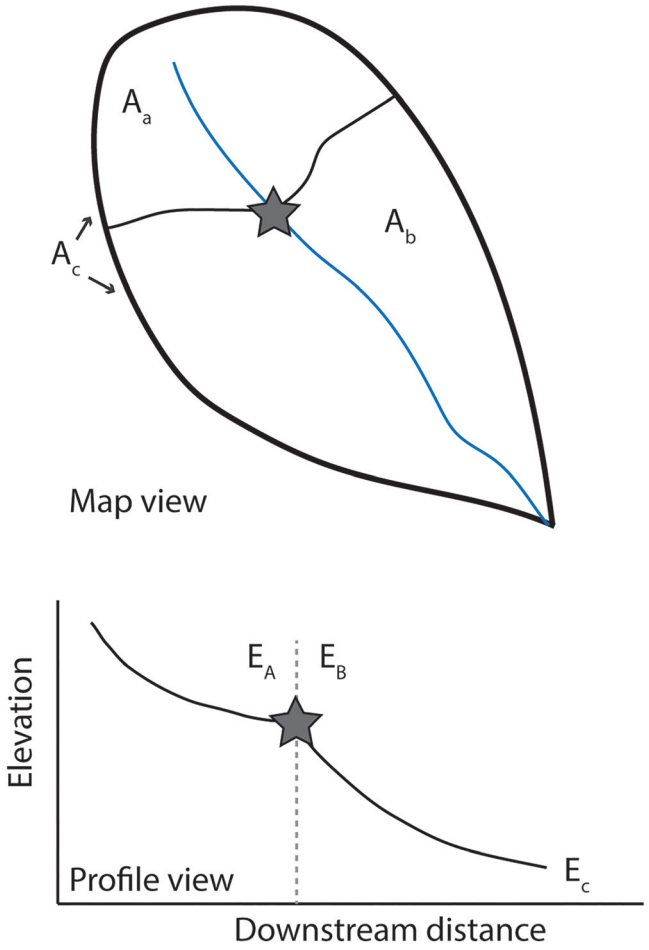

FIGURE 4 Conceptual diagram showing how different erosional zones add together to define total erosion rate at sample location. Top, a map view of a two zone mixing model showing the catchment areas above, Aa, and below, Ab, the knickpoint comprising the total catchment area Ac. Below, a topographic profile showing how the different zones relate to the transient river long profile with the samples collected at the knickpoint (star), EA, and at the river mouth, EC, allowing the determination of the erosion rate of only the transient, incising reach EB (modified from Rosenkranz et al. (2018). [Color figure can be viewed at wileyonlinelibrary.com]

3.3 | Calculation of unit stream power

Geomorphic indices were calculated using ArcGIS Pro and TAK (Forte & Whipple, 2018), k_{sn} values were determined with a $\Theta_{ref} = 0.45$ following Kent et al. (2017, 2021) and the profiler function. While the choice of reference concavity can impact the resultant k_{sn} values, Gailleton et al. (2021) demonstrated this is not significant.

Kent et al. (2021) constrained the rock strength (using Schmidt hammer rebound and Selby Rock Mass strength [SRMS]) and specific bedrock erodibility, E, using the unit stream power model (c.f. Whittaker et al., 2007; Attal et al., 2011; Zondervan, Whittaker, et al., 2020):

$$E = k_b \omega = k_b \frac{\rho g Q S}{W}, \quad (2)$$

where the unit stream power, ω represents energy dissipation per unit channel area on the bed with units of Wm^{-2}, ρ is the density of water, g is the acceleration due to gravity, Q is the water discharge (m^3s^{-1}), S is local channel slope (m/m) and W the channel width (m) as measured in the field. Consequently, specific bedrock erodibility, k_b, has units of ms^2kg^{-1}, representing the inverse of stress (c.f. Yanites et al., 2017).

Kent et al. (2021) demonstrate that the metamorphic rocks are around twice as hard as the sedimentary rocks. This difference is reflected by the bedrock erodibility, which was calculated as $2.2–6.3 \times 10^{-14}$ ms^2kg^{-1} in the metamorphic rocks. In contrast, bedrock erodibility values in the sedimentary units were 5 to 30 times larger (i.e. 5 to 30 times weaker) at 1.2×10^{-13} to 1.5×10^{-12} ms^2kg^{-1} (Kent et al., 2021). Significantly, stream power was shown to scale with fault throw rate in the metamorphic rocks but not in the sedimentary units; potentially because the weaker sedimentary rocks themselves directly influence the fluvial processes and long-term erosional dynamics.

However, values for unit stream power (Equation 2) for each river with reported CRN concentrations are required. Using the regional Q to A relationship determined using field measurements for the six rivers detailed in Kent et al. (2021), the estimate of Q for each river is found by extracting cumulative catchment area downstream along each sampled river at 100 m intervals using ArcGIS Pro 2.6.2 and the ALOS World 3D30 DEM. Similarly, the elevation is extracted at each point allowing the determination of local channel slope over each 100 m interval. The vertical accuracy of the AW3D30 DEM is <5 m (Tadono et al., 2016). As field-derived measurements of width are not available for all rivers, width is calculated using the scaling relationships of Finnegan et al. (2005) and Whittaker et al. (2007) as well as using Kent et al.'s (2021) local hydraulic scaling relationship (see Supporting Information for more detail). These estimates of width are then used to derive the downstream distribution of unit stream power, ω, for each river. The maximum stream power was found for each river, and an average of the three stream powers taken. The error reported is the 2σ value on these values.

3.4 | Rock strength and erodibility measurements

In situ rock strength measurements can be used to estimate bedrock erodibility, which is related to the inverse of the lithologies tensile strength (Sklar & Dietrich, 2001). However, tensile strength measurements are difficult to measure in the field and, as a result, the Schmidt hammer is commonly utilised owing to the ease of use and portability (e.g. Goudie, 2016). Kent et al. (2021) used an N-type Schmidt hammer to characterise average bedrock uniaxial compressive strength for each lithological unit. Additionally, information on fracture characteristics was collected to calculate the semi-quantitative SRMS (Selby, 1980).

Twenty Schmidt hammer readings were taken at 130 locations along the six study rivers, the majority of which are from the metamorphic basement. At only eight locations could the Schmidt hammer reliably return a rebound value for the sedimentary rocks. At another 28 sites, the exposed bedrock was too weak to accurately characterise the strength using this method and was recorded as having a rebound strength of <20 (the effective limit of the Schmidt hammer), allowing the SRMS to be determined even where bedrock is very weak. Schmidt hammer rebound and SRMS are then averaged for the ~2 km upstream of the CRN sample locations where possible.

4 | RESULTS

4.1 | ^{10}Be and ^{26}Al concentrations and catchment-wide erosion rate

The ^{10}Be concentrations measured in the new samples range from 1.3–10.0 × 10^4 atoms g^{-1}, while there were between 1.6–96.4 × 10^4 atoms g^{-1} of ^{26}Al (Table 1). These values compare well to previously reported CRN concentrations of ^{10}Be in the range 1.5–13.7 × 10^4 atoms g^{-1} (Table S1) from sediment in rivers mainly draining the metamorphic basement (Buscher et al., 2013; Heineke et al., 2019).

Therefore, apparent denudation rates range between 36 to 363 mMyr^{-1} and 40 to 3060 mMyr^{-1} for ^{10}Be and ^{26}Al, respectively. However, the denudation rates estimated from both nuclides agree within error for <30% of the samples. These samples show ^{26}Al/^{10}Be ratios in the range 6.2–7.8. The samples with a larger deviation between the derived denudation rates of each nuclide have significantly depleted ^{26}Al/^{10}Be ratios of <5.2 (Table 2). In a two-isotope diagram (Figure 5), 44% of data points cluster in the 0–0.5 Ma burial zone, 17% in the 0.5–1 Ma burial zone and 39% of points in the >1 Ma burial zone. These data indicate that a simple exposure/denudation history, without taking into account sediment storage, is incorrect for the majority of samples and implies that sediment reworking from the alluvial plain and/or the uplifted sediments is contributing a significant component of the transported bedload in many rivers (c.f. Granger, Kirchner, & Finkel, 1996).

Therefore, the ^{26}Al data allows the calculation of an average burial history and the determination of a new erosion rate taking into account the depletion of the ^{10}Be and ^{26}Al concentration during the time that the quartz grains were buried (Table 2). This calculation gives 'burial-corrected' erosion rates of 32 to 248 mMyr^{-1} for the study area catchments. Unfortunately, a similar calculation cannot be undertaken on the existing published CRN datasets (Buscher et al., 2013; Heineke et al., 2019) as there are no reported ^{26}Al data. As these sites are predominantly located in the footwall of the detachment fault, where there is little or no outcrop of sediments, it suggests that sediment storage should be limited for these samples. However, the presence of Holocene or older sediments in some catchments is a source of potential error that cannot be accounted for in the previously published data and may explain why the published erosion rates are, in general, slightly higher than those reported here. This hypothesis is supported by the ^{26}Al/^{10}Be ratios of three of samples upstream of the boundary between the sedimentary rocks and the Menderes Massif metamorphics falling in the >1 Ma burial zone (Figure 5).

On five rivers, samples were taken at or upstream of the slope-break knickpoint (TR18-01; 03; 07; 14; 18). These samples represent the denudation rate prior to landscape rejuvenation and transient river incision, as a result of fault linkage ~0.8 Ma (Kent et al., 2017), providing constraints for the unmixing model to determine the rate of erosion excluding these low erosion rate areas. Samples TR18-03 and TR18-07 give the lowest burial-corrected erosion rates at 32 and 60 mMyr^{-1}, respectively. Ridge crest erosion rates determined by Heineke et al. (2019) also fall in the range ~30–90 mMyr^{-1}. Whereas, samples TR18-01 and TR18-18 give much higher rates of 174 and 248 mMyr^{-1}, respectively; while TR18-14 returns an intermediate value of 119 mMyr^{-1}. Significantly, these latter three samples have only small catchment areas upstream of the sample point (1.7–3 km^2), which may be below a threshold for an appropriate size of catchment area. Additionally, the CAER from ^{10}Be and ^{26}Al nuclides are not within error and consequently indicate variable sediment recycling, which is difficult explain in the metamorphic headwaters. Therefore, given the higher values than for the ridge crests, small catchment areas and incomplete mixing, these latter three samples are not used to determine the erosion rate upstream of the knickpoint. Instead, the average of the other two samples is taken to be representative of the low incision zone and used for all catchments (c.f. Roda-Boluda et al., 2018). Therefore, the average CAER used is 46 mMyr^{-1} above the knickpoints.

4.2 | Results from unmixing model

In a landscape experiencing transient river incision, erosion rates above the knickpoint are expected to be lower than below the knickpoint. Therefore, we used an unmixing method (e.g. Granger, Kirchner, & Finkel, 1996; Rosenkranz et al., 2018) to remove the influence of such low erosion rates on downstream samples. Using the minimum erosion rate estimate determined above (i.e. 46 mMyr^{-1}), it is possible to derive a quantitative estimate for the erosion rates within the transient reach; that is, upstream of the active fault and downstream of the knickpoint. This method is applied to both the new burial-corrected CAER and also the previously published CRN datasets (Table 3). The effect of applying this unmixing model is variable depending on the proportion of the total catchment area falling in the low erosion rate zone above the knickpoint, and on the difference between the low erosion rate and the denudation rate determined for the downstream sample (Table 3). For example, where the downstream initial burial-corrected CAER are relatively low (such as on the Bozdağ), the unmixing results in a small increase in CAER (e.g. from 63 to 99 mMyr^{-1}). But where the difference between the assumed upstream erosion rate of 46 mMyr^{-1} and the downstream sample is greater, the final calculated rate is markedly higher. For example, on the Gumuşçay, the initial burial-corrected CAER is 144 mMyr^{-1}, which increases to 1330 mMyr^{-1} after unmixing; a ten-fold increase. For the majority of samples, the rates do increase, but a limited number of samples from or close to the lithological boundary result in no or negligible change. This is because the measured rate is close to the low erosion rate value even though the samples are within the knickzone. For one sample, 14 T1 (Heineke et al., 2019), this adjustment results in a negative erosion rate. This CAER is not included in further analyses.

4.3 | Relationship between CAER and geomorphic indices

These calculations enable the comparison between erosion rates to a number of geomorphic and geologic measures (Table 4). The burial-corrected mixed rates (i.e. CAER for the entire catchment) and the burial-corrected unmixed rates for the transient reaches (with the area upstream of the knickpoint removed) are compared alongside the recalculated published CAER (Buscher et al., 2013; Heineke et al., 2019) and the published CAER unmixed for the low erosion rate area, to

TABLE 1 New ^{10}Be and ^{26}Al analytical and derived erosion rate data with no corrections for subcatchments or sediment recycling/burial.

	Location							
Sample	Latitude (°N)	Longitude (°E)	River name	River no (Kent)	Distance along strike (km)	Mean catchment elevation (m)[c]	Topographic shielding	^{10}Be production rate (at/g/yr)
TR18-01	38.44701	27.877054	Akçapınar	9	35.4	787	0.9898	7.6806
TR18-02	38.48295	27.843433	Akçapınar	9	35.4	704	0.9750	7.0490
TR18-03	38.4048	27.957544	Sart Çay	11	53.4	1002	0.9738	9.0573
TR18-04	38.46693	28.003768	Sart Çay	11	53.4	844	0.9746	7.9411
TR18-05	38.47295	28.024298	Sart Çay	11	53.4	854	0.9743	8.0088
TR18-06	38.4651	28.052513	Çaltili	13	56.3	1018	0.9608	9.0620
TR18-07	38.39361	28.079372	Bozdağ	15	60.3	1301	0.9663	11.4862
TR18-08	38.4457	28.114133	Bozdağ	15	60.3	1215	0.9639	10.6928
TR18-09	38.47007	28.106199	Bozdağ	15	60.3	1108	0.9640	9.8025
TR18-10	38.46108	28.160952	Gümüş Çayı	16	65.4	1149	0.9594	10.0898
TR18-11	38.42648	28.208946	Kabazlı	17	69	1347	0.9770	12.0506
TR18-12	38.46332	28.200208	Kabazlı	17	69	997	0.9736	9.0205
TR18-13	38.45042	28.252572	Yeşilkavak	18	73.7	983	0.9616	8.8043
TR18-14	38.36203	28.356265	Yeniköy	23	85	795	0.9775	7.6208
TR18-15	38.40754	28.369389	Yeniköy	23	85	526	0.9769	6.0361
TR18-16	38.31973	28.553925	Badınca	28	105.1	1051	0.9574	9.2513
TR18-17	38.32456	28.565227	Badınca	28	105.1	1034	0.9579	9.1283
TR18-18	38.28846	28.487471	Badınca	28	105.1	1165	0.9642	10.2264

[aa] ^{10}Be and ^{26}Al concentrations were measured by the 5-MV NEC Pelletron accelerator mass spectrometer (AMS) at SUERC (Xu et al., 2010). Measured ^{10}Be is normalised to the NIST_27900 standard with an assumed isotope ratio of 2.79×10^{-11} and equivalent to 07KNSTD within rounding error. ^{26}Al is normalised to Z92-0222 with a defined isotope ratio of 4.11×10^{-11} and is equivalent to KNSTD.

[bb] Denudation rates were calculated using the online CRONUS-Earth calculator v 3.0 (Balco et al., 2008) using the LSDn scaling and a sample density of 2.65 gcm^3.

[cc] Sample elevation and shielding were derived from the ALOS World3D 30 m digital elevation model.

TABLE 1 (Continued)

Sample	^{26}Al production rate (at/g/yr)	Measured concentrations[a]				Denudation rates (no corrections)[b]			
		^{10}Be concentration (atoms g^{-1})	Uncertainty in ^{10}Be concentration (atoms g^{-1})	^{26}Al concentration (atoms g^{-1})	Uncertainty in ^{26}Al concentration (atoms g^{-1})	^{10}Be (m Myr^{-1})	Internal uncertainty	^{26}Al (m Myr^{-1})	Internal uncertainty
TR18-01	53.9639	19 935	1483	107 543	14 843	236.0	17.6	316.0	43.6
TR18-02	49.5853	29 153	1527	207 696	21 774	150.0	7.9	150.0	15.8
TR18-03	63.4609	152 808	4001	964 210	51 577	36.1	1.0	40.1	2.2
TR18-04	55.7586	16 803	1251	68 007	9544	290.0	21.6	517.0	72.7
TR18-05	56.2268	13 521	1218	16 163	6201	363.0	32.8	3060.0	1180.0
TR18-06	63.4898	97 728	3043	405 368	27 218	56.3	1.8	94.5	6.4
TR18-07	80.1738	92 364	3127	531 175	34 773	72.9	2.5	88.3	5.8
TR18-08	74.7231	85 558	2677	508 773	33 300	73.9	2.3	86.8	5.7
TR18-09	68.5974	74 938	2245	462 547	30 666	78.1	2.4	88.6	5.9
TR18-10	70.5714	26 596	1521	124 819	14 650	222.0	12.7	339.0	39.9
TR18-11	84.0655	100 108	3106	586 261	36 870	70.2	2.2	83.6	5.3
TR18-12	63.2126	17 481	1299	65 090	9569	310.0	23.0	598.0	87.9
TR18-13	61.7107	45 207	1988	287 656	20 621	117.0	5.2	130.0	9.4
TR18-14	53.5361	17 675	1518	59 004	8148	265.0	22.8	576.0	79.6
TR18-15	42.5557	19 759	1384	42 834	7648	196.0	13.7	661.0	118.0
TR18-16	64.7776	38 592	1806	300 619	26 206	142.0	6.7	129.0	11.3
TR18-17	63.9307	45 977	2250	240 144	19 537	118.0	5.8	160.0	13.0
TR18-18	71.4968	22 853	1559	153 479	15 142	262.0	17.9	277.0	27.4

[a]^{10}Be and ^{26}Al concentrations were measured by the 5-MV NEC Pelletron accelerator mass spectrometer (AMS) at SUERC (Xu et al., 2010). Measured ^{10}Be is normalised to the NIST_27900 standard with an assumed isotope ratio of 2.79×10^{-11} and equivalent to 07KNSTD within rounding error. ^{26}Al is normalised to Z92-0222 with a defined isotope ratio of 4.11×10^{-11} and is equivalent to KNSTD.
[b]Denudation rates were calculated using the online CRONUS-Earth calculator v 3.0 (Balco et al., 2008) using the LSDn scaling and a sample density of 2.65 gcm^3.
[c]Sample elevation and shielding were derived from the ALOS World3D 30 m digital elevation model.

TABLE 2 $^{26}Al/^{10}Be$ ratios, burial age and recalculated total catchment erosion rates based upon burial corrections.

Sample name	$^{26}Al/^{10}Be$ ratio	Burial age (Ma)	Burial corrected erosion rate ($mMyr^{-1}$)
TR18-01	5.4 ± 0.9	0.60±0.41	174±45
TR18-02	7.1 ± 0.8	0.00±0.34	149±19
TR18-03	6.3 ± 0.4	0.21±0.25	32±5
TR18-04	4.0 ± 0.6	1.19±0.41	159±42
TR18-05	1.2 ± 0.5	4.40±1.03	40±19
TR18-06	4.1 ± 0.3	1.05±0.27	33±6
TR18-07	5.7 ± 0.4	0.39±0.27	60±11
TR18-08	5.9 ± 0.4	0.33±0.27	63±11
TR18-09	6.2 ± 0.5	0.26±0.27	69±12
TR18-10	4.7 ± 0.6	0.87±0.36	144±33
TR18-11	5.9 ± 0.4	0.36±0.26	59±10
TR18-12	3.7 ± 0.6	1.35±0.43	157±42
TR18-13	6.4 ± 0.5	0.22±0.28	105±20
TR18-14	3.3 ± 0.5	1.60±0.42	119±33
TR18-15	2.2 ± 0.4	2.49±0.48	56±16
TR18-16	7.8 ± 0.8	0.00±0.18	139±10
TR18-17	5.2 ± 0.5	0.62±0.30	86±17
TR18-18	6.7 ± 0.8	0.12±0.34	248±45

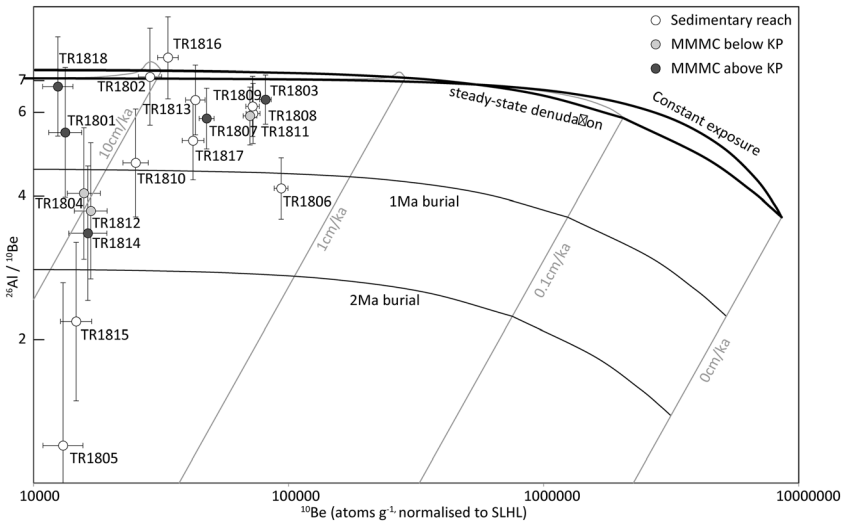

FIGURE 5 $^{26}Al/^{10}Be$ versus ^{10}Be ratio two isotope diagram showing burial model and concentration data scaled to surface production rates (Lal, 1991) for measured samples. Surface muon contributions of 0.99% ± 0.20% and 1.45% ± 0.29% were considered for ^{10}Be and ^{26}Al, respectively. Samples taken above the slope-break knickpoint are indicted by the grey symbols. MMMC = Menderes Massif Metamorphic core complex. Error bars include analytical and production rate uncertainties.

investigate the relationships between different factors and erosion along the southern margin of the Gediz Graben.

Firstly, if the along strike geomorphic character of the uplifted footwall of the Gediz Graben boundary fault is examined, it is clear that the mean catchment relief (Figure 6a), maximum incision (Figure 6b) and mean catchment slopes (Figure 6c) of sampled catchments are variable (Figure 6b) but overall follow the trend in fault throw rate (Figure 6b) with minima in these geomorphic metrics coinciding with the mapped fault segment boundaries (dashed lines, Figure 6). Indeed, the clear relationship along strike of the geomorphic expression of active faulting was partly used by Kent et al. (2016) to determine long-term uplift rates along the Gediz Graben boundary fault (Figure 6b). If the relief (Figure 6a) and slope (Figure 6c) above and below the knickpoints are considered separately, the same overall trends are apparent but with higher relief and slopes downstream of the knickpoint in the central and western parts of the range. This result is expected as the transient wave of incision causes gorge formation and hillslope steepening as it propagates through the river system. In the eastern part of the range, this relationship is apparently inverted with higher slopes and relief above the knickpoint. Although, fewer data are available in this zone.

When the normalised steepness index in the transient reach is plotted along strike, then the highest steepness indices are present in the centre of the fault array (Figure 6d), where current fault slip rates are highest. Maximum stream powers also cluster within the central fault segment, although it is important to acknowledge that lower values of steepness index and stream power are also present in the central part of the fault zone.

TABLE 3 Parameters used in the unmixing calculations to remove effect of low erosion rate and resultant erosion rates (Eb) for transient reach.

		Catchment area (m^2)			Erosion rates (LSDn)($mMyr^{-1}$)					
Sample no	River no	Aa	Ab	Ac	Ea	±	Ec	±	Eb	±
15 T10	1	23827405	19380606	43208011	46	14	55	7	65	23
15 T20	2	33018658	30633406	63652064	46	14	46	6	45	20
15 T19	2a	3713634	3729325	7442959	46	14	82	11	118	26
14 T1	4	12346068	4072945	16419013	46	14	33	4	-6	45
15 T21	7	5464432	16719167	22183599	46	14	79	10	90	14
15 T16	8	37403840	26672597	64076437	46	14	92	14	157	39
15 T17	8	3186523	815578.2	4002101	46	14	73	10	180	73
TR18-02	9	25649691	20803431	46453122	46	14	149	19	276	46
14 T2	9	25649691	20803431	46453122	46	14	187	37	361	84
17 T6	10	68662720	27467993	96130713	46	14	250	39	760	141
TR18-05	11	43799839	26295684	70095523	46	14	40	19	30	56
TR18-04	11	43799839	26295684	70095523	46	14	159	42	347	114
11 T1	13	45492741	35010065	80502806	46	14	60	7	77	24
TR18-06	13	45492741	35010065	80502806	46	14	33	6	16	23
TR18-09	15	47765237	22648803	70414040	46	14	69	12	118	48
TR18-08	15	47765237	22648803	70414040	46	14	63	11	99	45
TR18-10	16	30641229	5400620	59651748	46	14	144	33	1,330	373
11 T5	16	30641229	5400620	36041849	46	14	61	6	148	89
TR18-12	17	11032158	16141920	27174078	46	14	157	42	233	71
14 T3	17	11032158	11455766	22487924	46	14	151	22	252	45
TR18-11	17	11032158	5741419	16773577	46	14	59	10	84	40
11 T3	17	11032158	5558898	16591056	46	14	63	8	95	37
TR18-13	18	13303890	32870296	46174186	46	14	105	20	129	29
15 T15	18	13303890	32870296	46174186	46	14	239	43	317	61
11 T4	18	13303890	13624552	26928442	46	14	126	17	204	36
TR18-15	23	1932233	12999221	14931454	46	14	56	16	57	18
TR18-17	28	15970937	12825476	28796413	46	14	86	17	136	42
TR18-16	28	15970937	12219002	28189939	46	14	139	10	261	29

Note: Zone on determined erosion rates.

When the along strike trends in CAER are considered, there is an increase from the westernmost sample (54.5 $mMyr^{-1}$) into the centre of the range (250 $mMyr^{-1}$) for both the raw CAER and burial-corrected rates (Figures 6e and 7). However, rates then decrease again along two large river systems in the centre of the range (TR18-06, Catili and TR18-09, Bozdağ) before increasing again along the eastern part of the range. This decrease in erosion rates in the centre of the fault appears unexpected given these catchments are experiencing the highest uplift rates. When the unmixed CAER are plotted (Figure 6e), a clearer pattern of lower rates at the fault tips and higher rates in the centre of the range appears although the CAER in the centre of the fault are still generally subdued.

Interestingly, there are also differences in the CAER along individual sampled river systems with both decreasing and increasing erosion rates downstream being present (Figure 7). For example, and as expected, CAER increases along the Kabazlı River from 59 $mMyr^{-1}$ upstream of the Gediz Detachment fault to 157 $mMyr^{-1}$ at the boundary fault (Figure 7). By contrast, along the Badınca River (samples TR18-16 to TR18-18; easternmost river), burial-corrected erosion rates decrease downstream from ~250 $mMyr^{-1}$ in the headwaters to 86 $mMyr^{-1}$ upstream of the boundary fault. These data suggest that CAER do not scale simply with tectonic rates (c.f. Roda-Boluda et al., 2019) and may be influenced by factors such as sediment storage and contrasts in bedrock erodibility, which we evaluate below.

Secondly, the different CAER can also be compared with a range of topographic metrics that have previously been shown to correlate positively with erosion rates in previous studies such as relief and slope (i.e. Abbühl et al., 2011; Bellin, Vanacker, & Kubik, 2014; Kober et al., 2015; Miller et al., 2013). However, when the burial-corrected mixed rates (but not unmixed for low erosion rate areas) and published CAER data are plotted against mean catchment slope, topographic relief (150 m radius) and maximum incision depth upstream of the sample site, there are no trends (Figure S1).

By contrast, when these erosion rates are compared to the maximum upstream unit stream power, there is a significant ($p < 0.05$) positive linear trend with erosion rate in the published data from Heineke et al. (2019) (Figure 8a; $r^2 = 0.8$). There are also significant ($p < 0.05$) positive linear ($r^2 = 0.6–0.9$) relationships between erosion rates and

TABLE 4 Geomorphic and geological variables by sample and river.

River name	River no (Kent)	Sample	^{10}Be source	Distance along strike (km)	Catchment area (km^2)	Mean catchment slope (°)	Mean slope above KP (°)	Mean slope below KP (°)	Mean catchment relief (m)
Akçapınar	9	TR1801	This study	35.4	3	12.6	15.16	20.85	60
Akçapınar	9	TR1802	This study	35.4	46	16.7	15.16	20.85	78
Sart Çay	11	TR1803	This study	53.4	1	8.8	15.17	18.47	77
Sart Çay	11	TR1804	This study	53.4	5	17.5	15.17	18.47	77
Sart Çay	11	TR1805	This study	53.4	38	17.5	15.6	18.47	79
Çaltili	13	TR1806	This study	56.3	80	20.5	18.33	24.49	102
Bozdağ	15	TR1807	This study	60.3	34	20.3	18.33	22.02	96
Bozdağ	15	TR1808	This study	60.3	64	21.5	18.33	22.02	101
Bozdağ	15	TR1809	This study	60.3	70	19.3	18.33	22.02	99
Gümüş Çayı	16	TR1810	This study	65.4	60	21.7	22.41	20.75	106
Kabazlı	17	TR1811	This study	69	17	24.7	18.97	17.33	84
Kabazlı	17	TR1812	This study	69	28	17.6	18.97	17.33	84
Yeşilkavak	18	TR1813	This study	73.7	46	21.1	23.75	19.81	101
Yeniköy	23	TR1814	This study	85	3	16.7	18.28	16.34	88
Yeniköy	23	TR1815	This study	85	15	18.4	18.28	16.34	80
Badınca	28	TR1816	This study	105.1	2	23	24.97	19.4	111
Badınca	28	TR1817	This study	105.1	28	23	24.97	19.4	110
Badınca	28	TR1818	This study	105.1	29	21.5	24.97	19.4	105
Çay Sokak	10	17 T6	Heineke et al. (2019)	44.6	157	16	14.82	17.39	72
Armutlu	1	15 T10	Heineke et al. (2019)	5.6	70	21.9	14.85	26.27	101
Yeşilkavak	18	15 T15	Heineke et al. (2019)	73.7	3	22.1	23.75	19.81	102
Başiktaş Deresi	8	15 T16	Heineke et al. (2019)	32.9	104	16	15.17	16.41	73
Başiktaş Deresi	8	15 T17	Heineke et al. (2019)	32.9	7	9.4	15.17	12.81	73
Kazımpaşa	2a	15 T19	Heineke et al. (2019)	13.65	12	25.5	15.16	25.63	122
Yenikurudere	2	15 T20	Heineke et al. (2019)	12.8	104	24.2	19.06	27.03	114
Irlamaz Çayi	7	15 T21	Heineke et al. (2019)	22.7	36	21.7	15.17	23.02	98
Cevizdere	4	14 T1	Heineke et al. (2019)	17.7	28	22.4	18.09	24.52	107
Akçapınar	9	14 T2	Heineke et al. (2019)	35.4	69	17.1	15.16	20.85	76
Kabazlı	17	14 T3	Heineke et al. (2019)	69	1	24.7	18.97	17.33	82
Çaltili	13	11 T1	Buscher et al. (2013)	56.3	80	21.5	18.33	24.49	103
Kabazlı	17	11 T3	Buscher et al. (2013)	69	28	18.6	18.97	17.33	84

TABLE 4 (Continued)

River name	River no (Kent)	Sample	^{10}Be source	Distance along strike (km)	Catchment area (km^2)	Mean catchment slope (°)	Mean slope above KP (°)	Mean slope below KP (°)	Mean catchment relief (m)
Yeşilkavak	18	11 T4	Buscher et al. (2013)	73.7	42	24.9	23.75	17.33	102
Gümüş Çayı	16	11 T5	Buscher et al. (2013)	65.4	59	24.7	22.41	19.81	116

TABLE 4 (Continued)

River name	Mean catchment relief above KP (m)	Mean catchment relief below KP (m)	k_{sn} upstream of sample (m$^{0.9}$)	Error	Maximum stream power (Wm^{-2})	Error	Max incision upstream of sample (m)	Throw rate at fault since 0.7 ma (mMyr^{-1})	Long term throw rate since 2 ma (mMyr^{-1})
Akçapınar	66	101	45.0	1.9	1987	2314	132	1.41	0.44
Akçapınar	66	101	123.7		1987	406	356	1.41	0.44
Sart Çay	66	85	38.1	1.8	1792	2080	29	1.84	0.99
Sart Çay	66	85	142.3	1.0	1792	528	209	1.84	0.99
Sart Çay	66	85	142.3	1.0	1792	528	308	1.84	0.99
Çaltili	90	124	104.3		2600	704	615	1.91	1.28
Bozdağ	90	107	26.2	0.	6163	427	564	2	1.42
Bozdağ	90	107	165.5	5.4	6163	818	564	2	1.42
Bozdağ	90	107	165.5	5.4	6163	1198	564	2	1.42
Gümüş Çayı	112	100	75.8	1.8	3986	1060	634	1.86	1.33
Kabazlı	92	81	133.7	2.7	2376	1454	279	1.74	1.33
Kabazlı	92	81	137.7	2.7	2376	1439	331	1.74	1.33
Yeşilkavak	117	95	161.3	2.5	3274	1454	355	1.58	1.48
Yeniköy	88	78	84.7	2.0	1046	2080	211	1.3	0.99
Yeniköy	88	78	58.0	1.0	1046	2628	240	1.3	0.99
Badınca	125	93	138.8	0.7	2144	1060	442	0.72	0.59
Badınca	125	93	138.8	0.7	2144	1060	442	0.72	0.59
Badınca	125	93	80.5	1.7	2144	1416	300	0.72	0.59
Çay Sokak	69	83	184.4	2.7	3,838	1416	418	1.65	0.87
Armutlu	71	132	69.7	1.4	930	1416	722	0.7	0.7
Yeşilkavak	117	95	161.3	2.5	3274	1439	355	1.58	1.48
Başiktaş Deresi	66	78	94.4	2.0	1203	4343	372	1.35	0.9
Başiktaş Deresi	66	78	94.4	2.0	548	4343	70	1.35	0.9
Kazımpaşa	116	127	107.8	2.6	1192	4343	286	0.87	0.59
Yenikurudere	93	137	70.0	0.8	1023	2628	760	0.87	0.59

TABLE 4 (Continued)

River name	Mean catchment relief above KP (m)	Mean catchment relief below KP (m)	k_{sn} upstream of sample ($m^{0.9}$)	Error	Maximum stream power (Wm^{-2})	Error	Max incision upstream of sample (m)	Throw rate at fault since 0.7 ma ($mMyr^{-1}$)	Long term throw rate since 2 ma ($mMyr^{-1}$)
Irlamaz Çayi	77	111	91.7	0.7	1539	1454	289	1.1	0.71
Cevizdere	101	122	100.3	3.3	1998	1454	533	0.99	0.81
Akçapınar	66	101	123.7	3.2	1987	2080	356	1.41	0.44
Kabazlı	92	81	133.7	2.7	2376	631	331	1.74	1.33
Çaltili	90	124	104.3	2.2	2600	631	615	1.91	1.28
Kabazlı	92	81	133.7	2.7	2141	1282	279	1.74	1.33
Yeşilkavak	117	95	161.3	2.5	3274	1282	355	1.58	1.48
Gümüş Çayı	112	100	78.5	1.8	3986	1282	634	1.86	1.33

steepness index for the published data of Buscher et al. (2013) and Heineke et al. (2019) (Figure 8b) and a weak but significant linear relationship between erosion rates and throw rate on the graben boundary fault (Figure 8c; $r^2 = 0.2$). It is also noticeable that CAER expressed as $mMyr^{-1}$ are lower than the slip rates on the basin bounding fault, particularly towards the centre of the fault, where displacement rates are 2 mm yr^{-1} (i.e. 2000 $mMyr^{-1}$; Figure 6b).

Thirdly, the unmixed CAER that represent erosion rates only in the transient reach of the rivers can be compared with the same metrics. When these rates (which include published data as well as the new data determined here) are plotted against mean catchment slope, topographic relief and maximum incision depth upstream of the sample location, again there are no clear or significant trends (Figure S2). However, when unmixed CAER are compared to the upstream maximum unit stream power, there is a broad positive trend but with only a very weak correlation (Figure 9a). Although, when the Bozdağ samples are removed as potential outliers, because this river has very high stream power yet low erosion rates in the centre of the fault, a significant ($p < 0.05$) linear regression line with an $r^2 = 0.25$ can be plotted. Similarly, there is no trend between k_{sn} and CAER, but if the Gumusi cay sample is excluded as an outlier, there is weak ($r^2 = 0.28$) but significant ($p < 0.05$) positive relationship between erosion rates and steepness index with the best fit regression being an exponential trend (Figure 9b). When all unmixed CAERs are plotted against fault throw rate, there is no trend; however, when the samples from the detachment are removed so that only samples close to or at the boundary fault are retained, there is a weak ($r^2 = 0.1$) but not significant ($p > 0.05$) positive power law relationship between these two variables (Figure 9c).

4.4 | Relationship between rock strength, geomorphology and erosion rates

In order to assess the impact that the different bedrock lithologies have on the geomorphic response in the study region, the erosion rates for the different catchments can be compared to measurements of bedrock strength. The bedrock of the Bozdağ range can be broadly divided into the metamorphic lithologies of the Menderes Massif and the unconformably overlying Miocene and younger sediments. The metamorphic rocks are primarily composed of moderately strong to strong (c.f. Selby, 1980) schists, gneisses and granites where the SRMS > 60 (Figure 10a; c.f. Kent et al., 2021). By contrast, the syntectonic sandstones and conglomerates are weak to very weak (SRMS < 50). Therefore, if rock strength is the main control on CAER, then the harder metamorphic rocks should be eroding at a lower rate than the softer sediments.

Across the study region, the strong metamorphic rocks are located south of the Gediz Detachment in the upland regions of the Bozdağ range, while the weak sedimentary rocks are mainly to the north, that is, a soft over hard transition as represented in many landscape evolution models (e.g. Forte, Yanites, & Whipple, 2016). Interestingly though, when both measures of rock strength upstream of sample locations are compared to geomorphic variables such as relief (Figure 10b) and stream power (Figure 10c), there are no trends between the variables. This suggests that rock strength alone does not control relief or stream power. By contrast, there is a weak

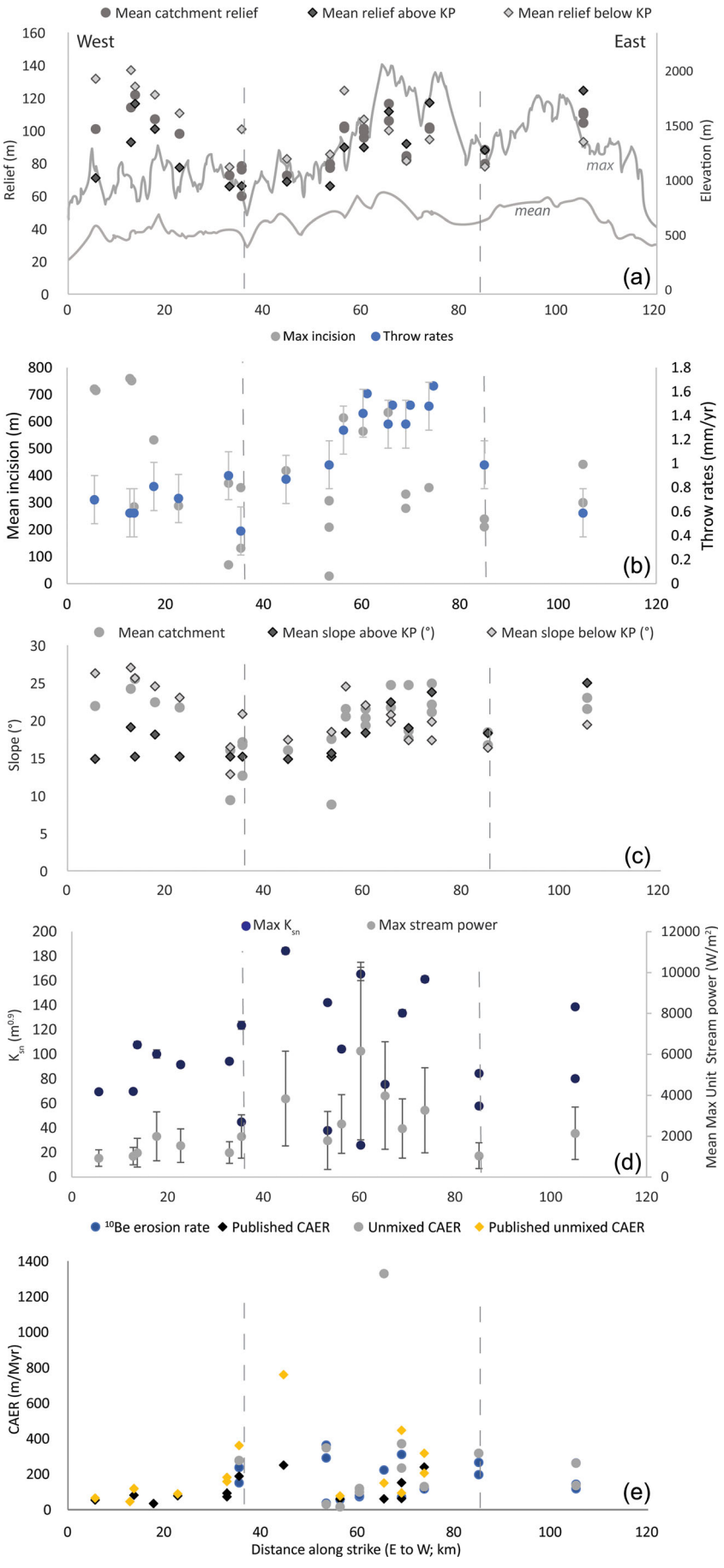

FIGURE 6 Along strike trends in geomorphic variables and catchment-averaged erosion rates (CAERs). Dashed lines show fault segment boundaries from Kent et al. (2017). (a) Catchment relief (mean whole catchment, mean above and below the tectonic knickpoint, and elevation mean and maximum swath profiles; (b) channel incision in the transient reaches and long-term throw rates (Kent et al., 2017); (c) total mean catchment slope and mean slope above and below the knickpoint; (d) normalised steepness index and maximum unit stream power, and (e) CAERs. *Note*: error bars are shown where greater than symbol size. [Color figure can be viewed at wileyonlinelibrary.com]

($r^2 \leq 0.2$) negative linear relationship between rock strength (SRMS and Schmidt hammer rebound) and the upstream steepness index, suggesting that rivers are on average less steep when the rocks are harder. However, this is not significant for either RMS or Schmidht Hammer rebound ($p > 0.05$) and is the opposite of the relationship that we would expect where the river is steeper in harder rocks.

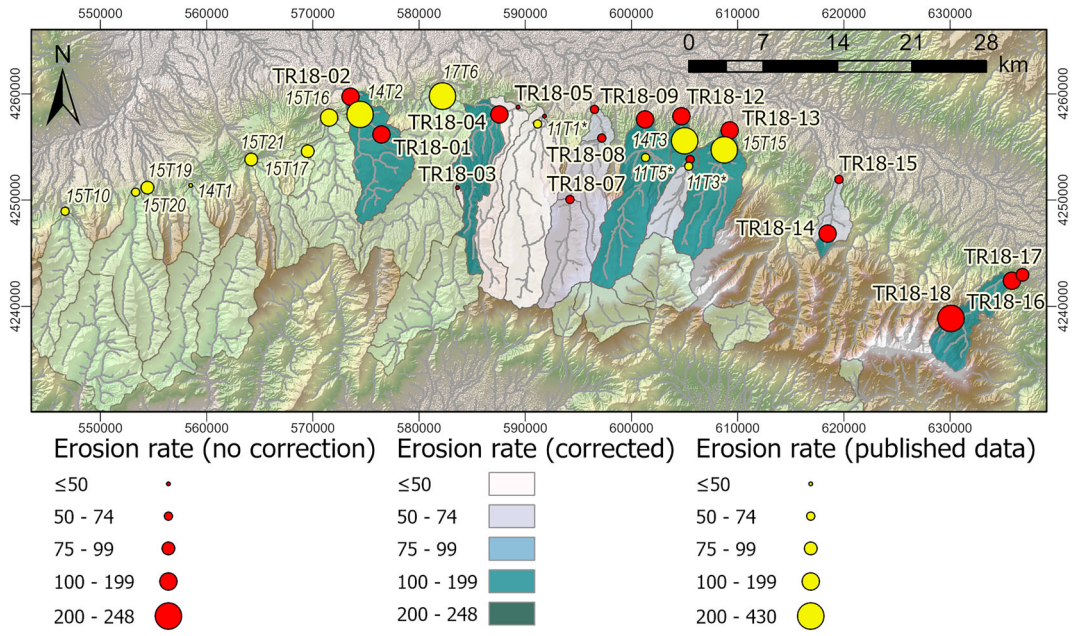

FIGURE 7 Map of showing the catchment-averaged erosion rates along the Gediz Graben Boundary Fault. Yellow circles show previously published data (Buscher et al., 2013; Heineke et al., 2019); while red circles show rates derived here but without correction for sediment storage and recycling. Rates corrected for these factors are shown by the shading of the catchment areas. [Color figure can be viewed at wileyonlinelibrary.com]

Furthermore, when CAERs are compared to the upstream rock strength, there is no clear relationship either for mixed or unmixed rates with both strong and weak rocks resulting in a similar range of CAERs (Figures 10e,f). Finally, there are no clear trends of these variables with uplift rate on the fault as indicated by the size of the symbols on Figures 10b–f.

5 | DISCUSSION

5.1 | What controls erosion rates along the margin of the Gediz Graben?

The geomorphology of the Bozdağ Range is shaped by the uplift along the Gediz Boundary fault and concomitant incision of the bedrock rivers resulting from the linkage of the boundary faults at ~0.8 Ma (Kent et al., 2017). Therefore, it is expected that there should be scaling relationships between various landscape metrics, uplift and erosion, similar to other regions around the world. For example, many studies show a positive relationship between CAER and catchment slope (i.e. Bellin, Vanacker, & Kubik, 2014; Roda-Boluda et al., 2019; Rosenkranz et al., 2018; Rossi et al., 2017) as well as positive relationship with channel steepness (Bellin, Vanacker, & Kubik, 2014; Cyr et al., 2010; DiBiase et al., 2010; Harkins et al., 2007; Miller et al., 2013; Rossi et al., 2017), which has been shown to be linear at low rates and steepness but becoming non-linear above a threshold steepness index. Related to landscape steepness is relief, which can either be measured as topographic relief across the catchment, or following Roda-Boluda et al. (2018) as maximum incision depth (i.e. maximum local relief) along the river. In both measures, CAER have previously been shown to have a positive relationship with these factors. For example, Bellin, Vanacker and Kubik (2014) demonstrated a positive linear relationship with relief and Roda-Boluda et al. (2018) a positive power law relationship with maximum incision depth. This is not unexpected assuming little pre-existing topography, as areas of higher relief will have had more material eroded than areas of lower relief over the same time span; thus, erosion rates should be higher where relief is higher. Though it is important to note that, in general, hillslopes have longer response times than rivers to changes in base-level (Schlunegger et al., 2013; Simpson & Schlunegger, 2003).

Unexpectedly, these trends appear not to hold true along the Bozdağ range either locally or catchment-wide, with no strong trends between erosion rates and average catchment slope, catchment relief or incision depth in either burial corrected CAER or unmixed for just the transient reach. While there are weak positive relationships observed in the data between CAER and normalised steepness index in the channel upstream of the sample point, this varies between a linear relationship for the whole CAER (not significant) and a weak but significant exponential for the transient reach only. The strongest and most significant of these weak trends is the linear relationship between the stream power and CAER (both burial-corrected and unmixed) albeit with larger uncertainties on the stream power data. These last two observations indicate that at the catchment scale and at the precision of our data, the rivers are broadly in line with a simple form of the stream power law, which is linear and $n = 1$ (Whipple & Tucker, 1999) where $E \approx KA^mS^n$ and is consistent with the analyses of Kent et al. (2021).

When CAER are compared to throw rates, it is striking that erosion rates are around an order of magnitude lower than uplift rate. Given the presence of knickpoints and a documented transient landscape response (Kent et al., 2017; Kent et al., 2021) demonstrating that this region is not in topographic steady state, this relationship is to be expected. As a result, the Bozdağ region will be experiencing surface uplift (Figures 8c and 9c). Yet, there are only weak positive relationships between the throw rate and CAERs, when corrected for sediment storage and for the presence of low relief zones.

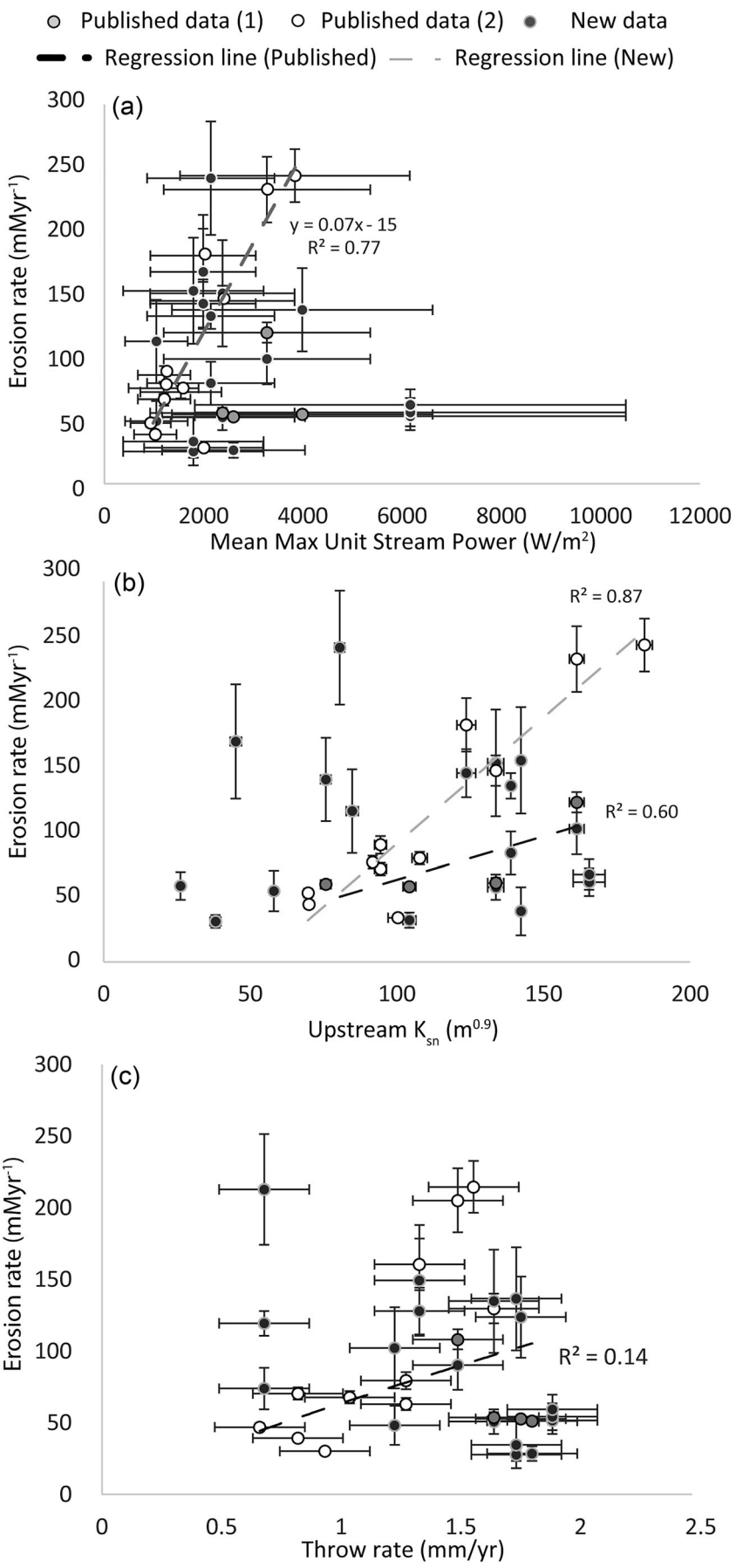

FIGURE 8 Comparison of geomorphic variables (a) mean maximum unit stream power and (b) normalised steepness index upstream, and (c) throw rate on the Gediz Graben Boundary Fault against catchment-averaged erosion rates for previously published data (1: Buscher et al., 2013; 2: Heineke et al., 2019) with internal uncertainty and for all samples collected here corrected for burial and sediment storage with calculated errors but not unmixed further.

Additionally, it is striking that these relationships are only significant for the burial-corrected CAERs, not for the unmixed CAERs. However, this apparent contradiction is consistent with the documented fault linkage. After a fault linkage event, the highest erosion rates should be present in the linkage zones where the previous minimum in fault throw (as these were the tips of individual faults) have had to rapidly

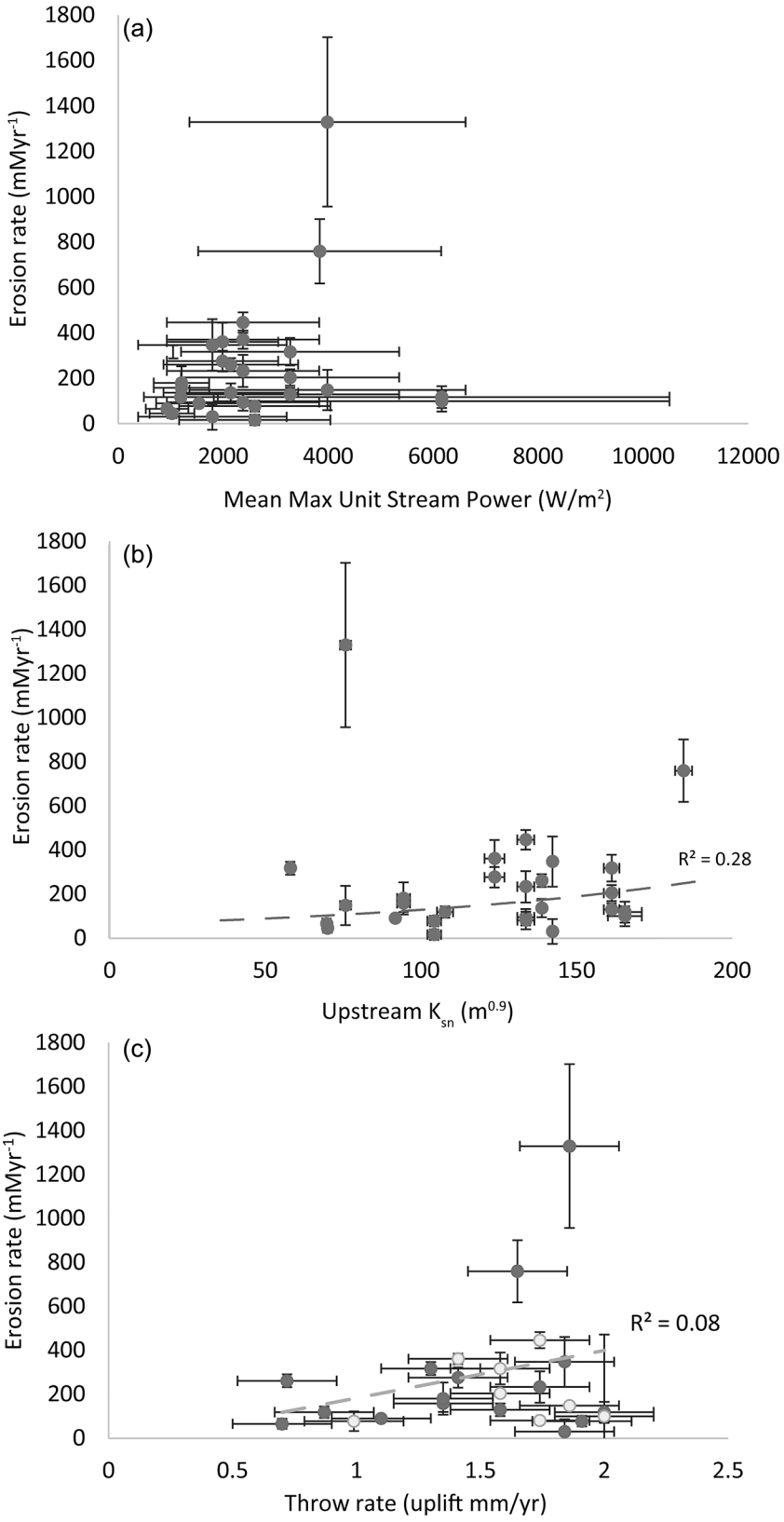

FIGURE 9 Comparison of geomorphic variables (a) maximum stream power and (b) upstream steepness index, and (c) throw rate on the Gediz Graben Boundary Fault against catchment-averaged erosion rate for previously published data and for samples collected here unmixed to remove the effect of the low erosion rate areas above the knickpoint. On C data have been separated into samples at the range front (dark) and at the detachment fault (light) to investigate the potential difference in erosion rates depending on the bedrock lithology.

increase to achieve the ideal fault profile (Kent, 2015); higher uplift rates will also result in increased erosion in these zones. This will also result in the part of the fault with the highest slip rates experiencing lower erosion rates, and as a result in the transient, reaches throw rate will not scale with erosion rate. Interestingly, at a catchment level, the CAERs do scale with throw rate but the correlation is weak, perhaps suggesting that prior to fault linkage throw rate did correlate with erosion rate.

A number of factors may cause the scatter and the weak correlations in these data, which we explore below. One complication to consider is that the results could be affected by sediment storage or non-uniform erosion as a result of landsliding (e.g. Binnie et al., 2006; Kober et al., 2012; Roda-Boluda et al., 2018). Neither of these factors appear to be likely along the Bozdağ range as firstly, the potential effect of sediment storage has been corrected through the inclusion of ^{26}Al CRN data. Secondly, there is little evidence for

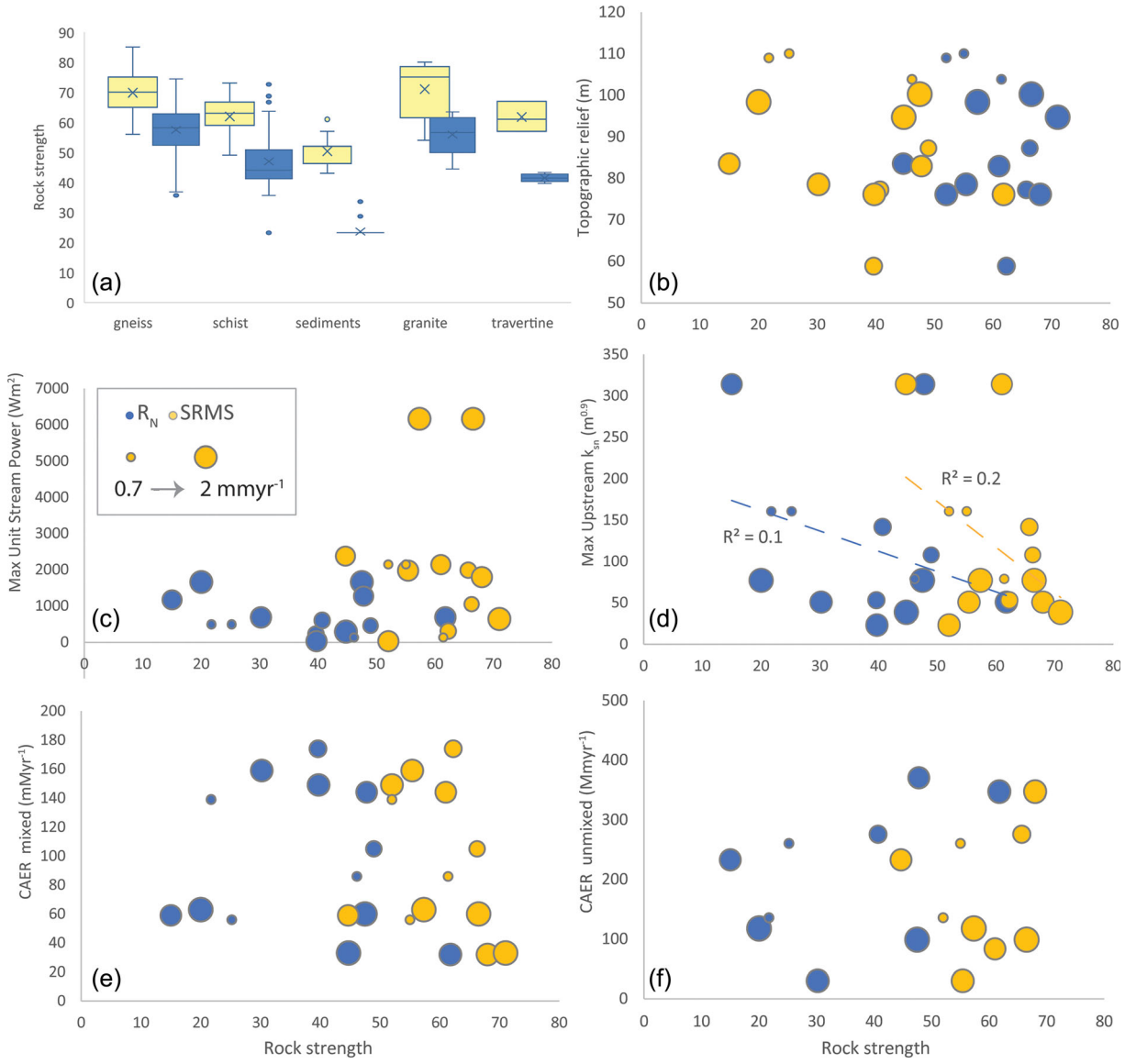

FIGURE 10 (a) Total Schmidt hammer rebound and SRMS for the main lithologies present in the study area. Schmidt hammer and SRMS calculated over 2 km upstream of the sample locations on the six main study rivers plotted against: (b) topographic relief; (c) maximum stream power; (d) upstream normalised steepness index; (e) catchment-averaged burial corrected erosion rates, and (f) unmixed erosion rates for the transient reach of the rivers. On B-E the size of the circle proportionally represents the throw rate at the range front where the largest circles equal 2 mmyr^{-1}. [Color figure can be viewed at wileyonlinelibrary.com]

significant landsliding in the study region to deliver material with sufficiently low ^{10}Be concentrations to perturb the measured river sediment concentrations. Incomplete sediment mixing could also explain the scatter in the data, while the measured CRN concentrations of repeat samples along several river systems are within 2σ error; we have limited data across the entire range to fully assess this issue, which has been shown to be a complicating factor in mountainous catchments elsewhere (Binnie et al., 2006).

Alternatively, the presence of inherited topography may play a significant role in the landscape response to uplift (c.f., Densmore et al., 2009). This explanation is supported by the clear imprint of the fault segments in the topographic metrics and the observation that in the eastern part of the range higher slopes and relief are found upstream of the tectonic knickpoint (Figure 6), despite transient river incision downstream of the knickpoint. Therefore, inherited topography might explain the disconnect between erosion rates and catchment wide variables such as slope and relief and potentially the variability in the CAER derived from the five samples taken from at or above the knickpoint. Yet, if this explanation was the only confounding factor, the unmixed CAER data should show stronger correlations with stream power and steepness index in particular, as the effect of low relief/low erosion rate zones have been accounted for in this calculation, and burial-corrected CAER for the whole catchments might be expected to show relationships with catchment mean slope or relief, which they do not. Therefore, another explanation for the spread in the data could be the influence of a strong lithological contrast within the catchments, which is discussed further below.

5.2 | The role of rock strength and lithology

A number of recent models have explored the impact of lithological variability on river evolution and erosion rates that could be used to

understand the relationships between CAER and the topographic metrics. Forte et al.'s (Forte, Yanites, & Whipple, 2016) model of using two distinct lithologies is highly applicable to the Gediz Graben. Their work demonstrated that when soft rocks overlie hard rocks along downstream dipping contact, the lithological contact becomes an important and persistent topographic feature in the landscape with the contact's dip-slope being preserved. This can clearly be seen in the study area as the Gediz Detachment is a pervasive feature along much of the range, and in many interfluve areas, the detachment is well preserved with little evidence of deep erosion.

Indeed, the presence of a very strong but thin cataclasite band found along the low-angle Gediz Detachment was used by Heineke et al. (2019) to explain the presence of low erosion rates and gentle slopes. In addition, they proposed that 'weak' phyllites and schists result in higher erosion rates in the centre of the range. The results presented here do not support this latter point, as lower CAERs are found in the centre of the range (Figure 7) and Figure 10e,f shows that the CAERs are invariant with rock strength upstream of the sample location despite a two-fold difference in strength between the sedimentary and metamorphic rocks overall (Figure 10a) and associated differences in erodibilty (Kent et al., 2021). This contradiction speaks to the difficulty in accurately constraining rock strength and erodibility in the field, determining the best categorisation, and linking such data to observed changes in fluvial behaviour and erosion rates (e.g. Bursztyn et al., 2015; Zondervan, Stokes, et al., 2020; Zondervan et al., 2020).

In addition, Forte et al.'s (Forte, Yanites, & Whipple, 2016) landscape evolution model also suggests that although the lithological boundary moves downstream over time, the erosion rates above and below the boundary will diverge. The soft rocks downstream will erode at the imposed uplift rate while the underlying hard rocks erode at a rate lower than the regional uplift rate. Another implication of Forte et al.'s (Forte, Yanites, & Whipple, 2016) landscape evolution model is that CAER would be perturbed or amplified downstream as a result of the lithological variation. We see that erosion rates of the underlying hard metamorphic rocks are eroding at rates lower than inferred uplift rates (Figure 9c), consistent with the landscape evolution model outputs. However, the erosion rates in the sedimentary bedrock reaches are also much lower than uplift rates at the graben boundary fault (Figure 9c), and only weakly and not significantly scale with throw rates on the fault.

Interestingly, Kent et al. (2021) demonstrated that stream power scales with uplift rate in the metamorphic bedrock reaches of their six study rivers. But uplift does not scale with stream power in the sedimentary reaches where sediment transport appears to be more important, resulting in a difference in the fluvial response in these reaches owing to the abundance of sedimentary material entering the river system (Kent et al., 2021). Therefore, while erosion rates in the sedimentary reaches still weakly, scale with the uplift rate the influence of sediment transport and hybrid or transport-limited nature of these lower reaches causes the erosion rate to be lower. In this study area, the lithological control on landscape evolution is therefore manifested not as bedrock erodibility but in variable fluvial responses that are not captured in a detachment-limited landscape evolution model. A key challenge for the future is to understand how the spatially variable erosion rates captured here are integrated over time to produce a coherent relief and sediment flux signal.

6 | CONCLUSIONS

Eighteen samples were collected for ^{10}Be and ^{26}Al cosmogenic nuclide analysis and combined with a further 15 previously published ^{10}Be concentrations (Buscher et al., 2013; Heineke et al., 2019) to determine CAERs along strike of the well-constrained Gediz Fault system in western Türkiye. This area features a significant lithological contrast where soft sediments overlie hard metamorphic rocks along a moderately dipping downstream contact; a series of north-flowing rivers are incising through this contact as a result of uplift along the fault at rates of up to 2 mMyr^{-1} and a fault-linkage event at ~0.8 Ma (Kent et al., 2017). This natural laboratory allows the results of recent landscape evolution models investigating the role of such lithological contrasts to be tested. The background rate of erosion of the pre-incision landscape is determined as 46 ± 46 mMyr^{-1} and erosion rates within the transient reach vary from 16 to 1330 mMyr^{-1}. Although, erosion rates weakly scale with unit stream power, steepness index and slip rate on the bounding fault, there are no clear relationships between erosion rate and relief or catchment slope. Catchment-wide and within the transient reach erosion rates are an order of magnitude lower than slip rates for both metamorphic, and sedimentary reaches and despite a 30-fold difference in erodibility, there is no difference in the erosion rate between strong and weak rocks. This finding is at odds with the results of landscape evolution modelling and is likely owing to the influence of sediment transport on fluvial dynamics in the sedimentary reaches, that is, some rivers are not completely detachment-limited. While the weak relationships between other variables remain unexplained but maybe the result of incomplete sediment mixing or the influence of pre-existing topography prior to the onset of the current incisional phase. These findings indicate that the erosional response to uplift along an active normal fault is a complex response to multiple drivers that vary spatially and temporally.

ACKNOWLEDGEMENTS

We acknowledge NERC Facilities grant (CIAF/9189/1018) for the cosmogenic analysis and Geological Society field work grant both awarded to S.J. Boulton that supported this research. The code used to calculate the burial corrected erosion rates using both ^{10}Be and ^{26}Al can be found at: https://github.com/angelrodes/banana1026. Figure 5 was plotted using CosmoCalc (Vermeesch, 2007) available for download from https://www.ucl.ac.uk/~ucfbpve/cosmocalc/.

CONFLICT OF INTEREST STATEMENT

None.

DATA AVAILABILITY STATEMENT

The authors confirm that the data supporting the findings of this study are available within the article [and/or] its supplementary materials.

ORCID

Sarah J. Boulton https://orcid.org/0000-0002-8251-0025

REFERENCES

Abbühl, L.M., Norton, K.P., Jansen, J.D., Schlunegger, F., Aldahan, A. & Possnert, G. (2011) Erosion rates and mechanisms of knickzone retreat inferred from 10Be measured across strong climate gradients

on the northern and Central Andes Western escarpment. *Earth Surface Processes and Landforms*, 36(11), 1464–1473. Available from: https://doi.org/10.1002/esp.2

Adams, B.A., Whipple, K.X., Forte, A.M., Heimsath, A.M. & Hodges, K.V. (2020) Climate controls on erosion in tectonically active landscapes. Science. *Advances*, 6(42), eaaz3166.164. Available from: https://doi.org/10.1126/sciadv.aaz3166

Attal, M., Cowie, P.A., Whittaker, A.C., Hobley, D., Tucker, G.E. & Roberts, G.P. (2011) Testing fluvial erosion models using the transient response of bedrock rivers to tectonic forcing in the Apennines, Italy. *Journal of Geophysical Research, Planets*, 116(F2), 1–17. Available from: https://doi.org/10.1029/2010JF001875

Balco, G., Stone, J.O., Lifton, N.A. & Dunai, T.J. (2008) A complete and easily accessible means of calculating surface exposure ages or erosion rates from 10Be and 26Al measurements. *Quaternary Geochronology*, 3(3), 174–195. Available from: https://doi.org/10.1016/j.quageo.2007.12.001

Bellin, N., Vanacker, V. & Kubik, P.W. (2014) Denudation rates and tectonic geomorphology of the Spanish Betic cordillera. *Earth and Planetary Science Letters*, 390, 19–30. Available from: https://doi.org/10.1016/J.EPSL.2013.12.045

Bernard, T., Sinclair, H.D., Gailleton, B., Mudd, S.M. & Ford, M. (2019) Lithological control on the post-orogenic topography and erosion history of the Pyrenees. *Earth and Planetary Science Letters*, 518, 53–66. Available from: https://doi.org/10.1016/J.EPSL.2019.04.034

Bierman, P.R., Marsella, K.A., Patterson, C., Davis, P.T. & Caffee, M. (1999) Mid-Pleistocene cosmogenic minimum-age limits for pre-Wisconsinan glacial surfaces in southwestern Minnesota and southern Baffin Island: a multiple nuclide approach. *Geomorphology*, 27(1-2), 25–39. Available from: https://doi.org/10.1016/S0169-555X(98)00088-9.

Binnie, S.A., Phillips, W.M., Summerfield, M.A. & Fifield, L.K. (2006) Sediment mixing and basin-wide cosmogenic nuclide analysis in rapidly eroding mountainous environments. *Quaternary Geochronology*, 1(1), 4–14. Available from: https://doi.org/10.1016/j.quageo.2006.06.013

Boulton, S.J. & Stokes, M. (2018) Which DEM is best for analyzing fluvial landscape development in mountainous terrains? *Geomorphology*, 310, 168–187. Available from: https://doi.org/10.1016/j.geomorph.2018.03.002

Bozkurt, E. (2003) Origin of NE-trending basins in western Turkey. *Geodinamica Acta'*, 16(2-6), 61–81. Available from: https://doi.org/10.1016/S0985-3111(03)00002-0.

Bozkurt, E., Sözbilir, I.R. & H. (2004) Tectonic evolution of the Gediz Graben: field evidence for an episodic, two-stage extension in western Turkey. *Geological Magazine*, 141(01), 63–79. Available from: https://doi.org/10.1017/S0016756803008379.

Bursztyn, N., Pederson, J.L., Tressler, C., Mackley, R.D. & Mitchell, K.J. (2015) Rock strength along a fluvial transect of the Colorado plateau–quantifying a fundamental control on geomorphology. *Earth and Planetary Science Letters*, 429, 90–100. Available from: https://doi.org/10.1016/j.epsl.2015.07.042

Buscher, J.T., Hampel, A., Hetzel, R., Dunkl, I., Glotzbach, C., Struffert, A., et al. (2013) Quantifying rates of detachment faulting and erosion in the Central Menderes massif (western Turkey) by thermochronology and cosmogenic 10 be. *Journal of the Geological Society of London*, 170(4), 669–683. Available from: https://doi.org/10.1144/jgs2012-132

Child, D., Elliott, G., Mifsud, C., Smith, A.M. & Fink, D. (2000) Sample processing for earth science studies at ANTARES. *Nuclear Instruments and Methods in Physics Research Section B: Beam Interactions with Materials and Atoms*, 172(1-4), 856–860. Available from: https://doi.org/10.1016/S0168-583X(00)00198-1

Çiftçi, N.B. & Bozkurt, E. (2009) Evolution of the Miocene sedimentary fill of the Gediz Graben, SW Turkey. *Sedimentary Geology*, 216(3), 49–79. Available from: https://doi.org/10.1016/j.sedgeo.2009.01.004.

Cyr, A.J., Granger, D.E., Olivetti, V. & Molin, P. (2010) Quantifying rock uplift rates using channel steepness and cosmogenic nuclide–determined erosion rates: examples from northern and southern Italy. *Lithosphere*, 2(3), 188–198. Available from: https://doi.org/10.1130/L96.1

D'Arcy, M. & Whittaker, A.C. (2014) Geomorphic constraints on landscape sensitivity to climate in tectonically active areas. *Geomorphology*, 204, 366–381. Available from: https://doi.org/10.1016/j.geomorph.2013.08.019

Darling, A., Whipple, K., Bierman, P., Clarke, B. & Heimsath, A. (2020) Resistant rock layers amplify cosmogenically-determined erosion rates. *Earth Surface Processes and Landforms*, 45(2), 312–330. Available from: https://doi.org/10.1002/esp.4730

Densmore, A.L., Hetzel, R., Ivy-Ochs, S., Krugh, W.C., Dawers, N. & Kubik, P. (2009) Spatial variations in catchment-averaged denudation rates from normal fault footwalls. *Geology*, 37(12), 1139–1142. Available from: https://doi.org/10.1130/G30164A.1

DiBiase, R.A., Whipple, K.X., Heimsath, A.M. & Ouimet, W.B. (2010) Landscape form and millennial erosion rates in the San Gabriel Mountains, CA. *Earth and Planetary Science Letters*, 289(1-2), 134–144. Available from: https://doi.org/10.1016/J.EPSL.2009.10.036

Duvall, A. (2004) Tectonic and lithologic controls on bedrock channel profiles and processes in coastal California. *Journal of Geophysical Research*, 109, F03002. Available from: https://doi.org/10.1029/2003JF000086.

Finnegan, N.J., Roe, G., Montgomery, D.R. & Hallet, B. (2005) Controls on the channel width of rivers: implications for modeling fluvial incision of bedrock. *Geology*, 33(3), 229–232. Available from: https://doi.org/10.1130/G21171.1

Forte, A.M. & Whipple, K.X. (2018) Criteria and tools for determining drainage divide stability. *Earth and Planetary Science Letters*, 493, 102–117. Available from: https://doi.org/10.1016/J.EPSL.2018.04.026

Forte, A.M., Yanites, B.J. & Whipple, K.X. (2016) Complexities of landscape evolution during incision through layered stratigraphy with contrasts in rock strength. *Earth Surface Processes and Landforms*, 41(12), 1736–1757. Available from: https://doi.org/10.1002/esp.3947

Gailleton, B., Sinclair, H.D., Mudd, S.M., Graf, E.L.S. & Mațenco, L.C. (2021) Isolating lithologic versus tectonic signals of river profiles to test orogenic models for the eastern and southeastern Carpathians. *Journal of Geophysical Research - Earth Surface*, 126(8), e2020JF005970. Available from: https://doi.org/10.1029/2020JF005970

Gessner, K., Piazolo, S., Güngör, T., Ring, U., Kröner, A. & Passchier, C.W. (2001) Tectonic significance of deformation patterns in granitoid rocks of the Menderes nappes, Anatolide belt, southwest Turkey. *International Journal of Earth Sciences*, 89(4), 766–780. Available from: https://doi.org/10.1007/s005310000106.

Goudie, A.S. (2016) Quantification of rock control in geomorphology. *Earth-Science Reviews*, 159, 374–387. Available from: https://doi.org/10.1016/J.EARSCIREV.2016.06.012

Granger, D., Kirchner, J. & Finkel, R. (1996) Spatially averaged long-term erosion rates measured from in situ-produced cosmogenic nuclides in alluvial sediment. *Journal of Geology*, 104(3), 249–257. Available from: https://doi.org/10.1086/629823

Granger, D.E. & Muzikar, P.F. (2001) Dating sediment burial with in situ-produced cosmogenic nuclides: theory, techniques, and limitations. *Earth and Planetary Science Letters*, 188(1-2), 269–281. Available from: https://doi.org/10.1016/S0012-821X(01)00309-0

Harkins, N., Kirby, E., Heimsath, A., Robinson, R. & Reiser, U. (2007) Transient fluvial incision in the headwaters of the Yellow River, northeastern Tibet, China. *Journal of Geophysical Research - Earth Surface*, 112(F3), 1–21. Available from: https://doi.org/10.1029/2006JF000570

Heineke, C., Hetzel, R., Nilius, N.-P., Glotzbach, C., Akal, C., Christl, M., et al. (2019) Spatial patterns of erosion and landscape evolution in a bivergent metamorphic core complex revealed by cosmogenic 10Be: the Central Menderes massif (western Turkey). *Geosphere*, 15(6), 1846–1868. Available from: https://doi.org/10.1130/GES02013.1

Kent, E., Boulton, S.J., Stewart, I.S., Whittaker, A.C. & Alçiçek, M.C. (2016) Geomorphic and geological constraints on the active normal faulting of the Gediz (Alaşehir) Graben, Western Turkey. *Journal of the Geological Society*, 173, 666–678. Available from: https://doi.org/10.1144/jgs2015-121.

Kent, E., Boulton, S.J., Whittaker, A.C., Stewart, I.S. & Cihat Alçiçek, M. (2017) Normal fault growth and linkage in the Gediz (Alaşehir) graben, Western Turkey, revealed by transient river long-profiles and slope-break knickpoints. *Earth Surface Processes and Landforms*, 42(5), 836–852. Available from: https://doi.org/10.1002/esp.4049

Kent, E., Whittaker, A.C., Boulton, S.J. & Alçiçek, M.C. (2021) Quantifying the competing influences of lithology and throw rate on bedrock river incision. *GSA Bulletin*, 133(7-8), 1649–1664. Available from: https://doi.org/10.1130/B35783.1

Kent, E.J. (2015) The relationship between active faulting and fluvial geomorphology: a case study in the Gediz Graben, Turkey. University of Plymouth, 397.

Kirby, E. & Whipple, K.X. (2012) Expression of active tectonics in erosional landscapes. *Journal of Structural Geology*, 44, 54–75. Available from: https://doi.org/10.1016/j.jsg.2012.07.009

Kober, F., Hippe, K., Salcher, B., Ivy-Ochs, S., Kubik, P.W., Wacker, L., et al. (2012) Debris-flow–dependent variation of cosmogenically derived catchment-wide denudation rates. *Geology*, 40(10), 935–938. Available from: https://doi.org/10.1130/G33406.1

Kober, F., Zeilinger, G., Hippe, K., Marc, O., Lendzioch, T., Grischott, R., et al. (2015) Tectonic and lithological controls on denudation rates in the central Bolivian Andes. *Tectonophysics*, 657, 230–244. Available from: https://doi.org/10.1016/j.tecto.2015.06.037

Lal, D. (1991) Cosmic ray labeling of erosion surfaces: in situ nuclide production rates and erosion models. *Earth and Planetary Science Letters*, 104(2–4), 424–439. Available from: https://doi.org/10.1016/0012-821X(91)90220-C

Miller, S.R., Baldwin, S.L. & Fitzgerald, P.G. (2012) Transient fluvial incision and active surface uplift in the Woodlark Rift of eastern Papua New Guinea. *Lithosphere*, 4(2), 131–149. Available from: https://doi.org/10.1130/L135.1

Miller, S.R., Sak, P.B., Kirby, E. & Bierman, P.R. (2013) Neogene rejuvenation of central Appalachian topography: evidence for differential rock uplift from stream profiles and erosion rates. *Earth and Planetary Science Letters*, 369–370, 1–12. Available from: https://doi.org/10.1016/J.EPSL.2013.04.007

Mitchell, N.A. & Yanites, B.J. (2021) Bedrock river erosion through dipping layered rocks: quantifying erodibility through kinematic wave speed. *Earth Surface Dynamics*, 9(4), 723–753. Available from: https://doi.org/10.5194/esurf-9-723-2021

Okay, A.I. & Satir, M. (2000) Coeval plutonism and metamorphism in a latest Oligocene metamorphic core complex in northwest Turkey. *Geological Magazine*, 137(5), 495–516. Available from: https://doi.org/10.1017/S0016756800004532.

Oner, Z. & Dilek, Y. (2011) Supradetachment basin evolution during continental extension: The Aegean province of western Anatolia. *Turkey. Geological Society of America Bulletin*, 123(11-12), 2115–2141. Available from: https://doi.org/10.1130/B30468.1.

Ortega, J.A., Wohl, E. & Livers, B. (2013) Waterfalls on the eastern side of Rocky Mountain National Park, Colorado, USA. *Geomorphology*, 198, 37–44. Available from: https://doi.org/10.1016/j.geomorph.2013.05.010

Ouimet, W.B., Whipple, K.X. & Granger, D.E. (2009) Beyond threshold hillslopes: channel adjustment to base-level fall in tectonically active mountain ranges. *Geology*, 37(7), 579–582. Available from: https://doi.org/10.1130/G30013A.1

Peifer, D., Persano, C., Hurst, M.D., Bishop, P. & Fabel, D. (2020) Growing topography due to contrasting rock types in a tectonically dead landscape. *Earth Surface Dynamics*, 2021(2), 167–181. Available from: https://doi.org/10.5194/esurf-9-167-2021

Perne, M., Covington, M.D., Thaler, E.A. & Myre, J.M. (2017) Steady state, erosional continuity, and the topography of landscapes developed in layered rocks. *Earth Surface Dynamics*, 5(1), 85–100. Available from: https://doi.org/10.5194/esurf-5-85-2017

Purvis, M. & Robertson, A. (2004) A pulsed extension model for the Neogene–Recent E–W-trending Alaşehir Graben and the NE–SW-trending Selendi and Gördes Basins, western Turkey. *Tectonophysics*, 391(1-4), 171–201. Available from: https://doi.org/10.1016/j.tecto.2004.07.011.

Purvis, M. & Robertson, A. (2005) Sedimentation of the Neogene–Recent Alaşehir (Gediz) continental graben system used to test alternative tectonic models for western (Aegean) Turkey. *Sedimentary Geology*, 173(1-4), 373–408. Available from: https://doi.org/10.1016/j.sedgeo.2003.08.005.

Regalla, C., Kirby, E., Fisher, D. & Bierman, P. (2013) Active forearc shortening in Tohoku, Japan: constraints on fault geometry from erosion rates and fluvial longitudinal profiles. *Geomorphology*, 195, 84–98. Available from: https://doi.org/10.1016/j.geomorph.2013.04.029

Ring, U.W.E., Johnson, C., Hetzel, R. & Gessner, K. (2003) Tectonic denudation of a Late Cretaceous–Tertiary collisional belt: regionally symmetric cooling patterns and their relation to extensional faults in the Anatolide belt of western Turkey. *Geological Magazine*, 140(4), 421–441. Available from: https://doi.org/10.1017/S0016756803007878.

Roda-Boluda, D.C., D'Arcy, M., McDonald, J. & Whittaker, A.C. (2018) Lithological controls on hillslope sediment supply: insights from landslide activity and grain size distributions. *Earth Surface Processes and Landforms*, 43(5), 956–977. Available from: https://doi.org/10.1002/esp.4281

Roda-Boluda, D.C., D'Arcy, M., Whittaker, A.C., Gheorghiu, D.M. & Rodés, Á. (2019) 10Be erosion rates controlled by transient response to normal faulting through incision and landsliding. *Earth and Planetary Science Letters*, 507, 140–153. Available from: https://doi.org/10.1016/j.epsl.2018.11.032

Rodés, Á. (2021) The NUNAtak ice thinning (NUNAIT) calculator for cosmonuclide elevation profiles. *Geosciences*, 11(9), 362. Available from: https://doi.org/10.3390/geosciences11090362

Rosenkranz, R., Schildgen, T., Wittmann, H. & Spiegel, C. (2018) Coupling erosion and topographic development in the rainiest place on earth: reconstructing the Shillong plateau uplift history with in-situ cosmogenic 10Be. *Earth and Planetary Science Letters*, 483, 39–51. Available from: https://doi.org/10.1016/j.epsl.2017.11.047

Rossi, M.W., Quigley, M.C., Fletcher, J.M., Whipple, K.X., Díaz-Torres, J.J., Seiler, C., et al. (2017) Along-strike variation in catchment morphology and cosmogenic denudation rates reveal the pattern and history of footwall uplift, Main gulf escarpment, Baja California. *Bulletin Geological Society of America*, 129(7-8), 837–854. Available from: https://doi.org/10.1130/B31373.1

Safran, E.B., Bierman, P.R., Aalto, R., Dunne, T., Whipple, K.X. & Caffee, M. (2005) Erosion rates driven by channel network incision in the Bolivian Andes. *Earth Surface Processes and Landforms: the Journal of the British Geomorphological Research Group*, 30(8), 1007–1024. Available from: https://doi.org/10.1002/esp.1259

Schlunegger, F., Norton, K., Caduff, R. & Shroder, J.F. (2013) Hillslope processes in temperate environments. *Treatise in Geomorphology*, 3, 337–354. Available from: https://doi.org/10.1016/B978-0-12-374739-6.00183-4

Schwanghart, W. & Scherler, D. (2014) TopoToolbox 2 – MATLAB-based software for topographic analysis and modeling in earth surface sciences. *Earth Surface Dynamics*, 2(1), 1–7. Available from: https://doi.org/10.5194/esurf-2-1-2014

Selby, M.J. (1980) A rock mass strength classification for geomorphic purposes: with tests from Antarctica and New Zealand. *Zeitschrift für Geomorphologie*, 24(1), 31–51. Available from: https://doi.org/10.1127/zfg/24/1984/31

Seyitoğlu, G. & Scott, B.C. (1996) Age of the Alaşehir graben (west Turkey) and its tectonic implications. *Geological Journal*, 31(1), 1–11.1. Available from: https://doi.org/10.1002/(SICI)1099-1034(199603)31:1<1::AID-GJ688>3.0.CO;2-S.

Seyitoğlu, G., Tekeli, O., Çemen, I., Sen, S. & Isik, V. (2002) The role of the flexural rotation/rolling hinge model in the tectonic evolution of the Alasehir graben, western Turkey. *Geological Magazine*, 139(01), 15–26. Available from: https://doi.org/10.1017/S0016756801005969.

Simpson, G. & Schlunegger, F. (2003) Topographic evolution and morphology of surfaces evolving in response to coupled fluvial and hillslope sediment transport. *Journal of Geophysical Research*, 108(B6), 2300. Available from: https://doi.org/10.1029/2002JB00216

Sklar, L.S. & Dietrich, W.E. (2001) Sediment and rock strength controls on river incision into bedrock. *Geology*, 29(12), 1087–1090. Available from: https://doi.org/10.1130/0091-7613

Snyder, N.P., Whipple, K.X., Tucker, G.E. & Merritts, D.J. (2000) Stream profiles in the Mendocino triple junction region, northern California. *GSA Bulletin*, 112(8), 1250–1263. Available from: https://doi.org/10.1130/0016-7606

Stolle, A., Schwanghart, W., Andermann, C., Bernhardt, A., Fort, M., Jansen, J.D., et al. (2019) Protracted river response to medieval earthquakes. *Earth Surface Processes and Landforms*, 44(1), 331–341. Available from: https://doi.org/10.1002/esp.4517

Sullivan, D.G. (1988) The discovery of Santorini Minoan tephra in western Turkey. *Nature*, 333(6173), 552–554. Available from: https://doi.org/10.1038/333552a0

Süzen, M.L., Toprak, V. & Rojay, B. (2006) High-altitude Plio–quaternary fluvial deposits and their implication on the tilt of a horst, western Anatolia, Turkey. *Geomorphology*, 74, 80–99. Available from: https://doi.org/10.1016/J.GEOMORPH.2005.07.012

Tadono, T., Nagai, H., Ishida, H., Oda, F., Naito, S., Minakawa, K., et al. (2016) Initial Validation of the 30 m-mesh Global Digital Surface Model Generated by ALOS PRISM. *The International Archives of the Photogrammetry, Remote Sensing and Spatial Information Sciences*, ISPRS, XLI-B4, 157–162. Available from: https://doi.org/10.5194/isprs-archives-XLI-B4-157-2016.

Ten Veen, J.H., Boulton, S.J. & Alçiçek, M.C. (2009) From Palaeotectonics to Neotectonics in the Neotethys Realm: The Importance of Kinematic Decoupling and Inherited Structural Grain in SW Anatolia (Turkey). *Tectonophysics*, 473(1–2), 261–281.

Vermeesch, P. (2007) CosmoCalc: An Excel add-in for cosmogenic nuclide calculations. *Geochemistry, Geophysics, Geosystems*, 8, Q08003. Available from: https://doi.org/10.1029/2006GC001530

von Blanckenburg, F. (2006) The control mechanisms of erosion and weathering at basin scale from cosmogenic nuclides in river sediment. *Earth and Planetary Science Letters*, 242, 224–239. Available from: https://doi.org/10.1016/j.epsl.2005.11.017.

Whipple, K.X. & Tucker, G.E. (1999) Dynamics of the stream-power river incision model: implications for height limits of mountain ranges, landscape response timescales, and research needs. *Journal of Geophysical Research - Solid Earth*, 104(B8), 17661–17674. Available from: https://doi.org/10.1029/1999JB900120

Whittaker, A.C. (2012) How do landscapes record tectonics and climate? *Lithosphere*, 4(2), 160–164. Available from: https://doi.org/10.1130/RF.L003.1

Whittaker, A.C. & Boulton, S.J. (2012) Tectonic and climatic controls on knickpoint retreat rates and landscape response times. *Journal of Geophysical Research - Earth Surface*, 117(F2), 117. Available from: https://doi.org/10.1029/2011JF002157

Whittaker, A.C., Cowie, P.A., Attal, M., Tucker, G.E. & Roberts, G.P. (2007) Bedrock channel adjustment to tectonic forcing: implications for predicting river incision rates. *Geology*, 35(2), 103–106. Available from: https://doi.org/10.1130/G23106A.1

Wobus, C., Whipple, K.X., Kirby, E., Snyder, N., Johnson, J., Spyropolou, K., et al. (2006) Tectonics from topography: Procedures, promise, and pitfalls. In: Willett, S.D., Hovius, N., Brandon, M.T. & Fisher, D.M. (Eds.) *Tectonics, climate, and landscape evolution*. Special Paper 398 Geological Society of America, Boulder, Colorado, USA. https://doi.org/10.1130/2006.2398(04)

Wolpert, J.A. & Forte, A.M. (2021) Response of transient rock uplift and base level knickpoints to erosional efficiency contrasts in bedrock streams. *Earth Surface Processes and Landforms*, 46(10), 2092–2109. Available from: https://doi.org/10.1002/esp.5146

Xu, S., Dougans, A.B., Freeman, S.P.H.T., Schnabel, C. & Wilcken, K.M. (2010) Improved 10Be and 26Al-AMS with a 5 MV spectrometer. *Nuclear Instruments and Methods in Physics Research Section B: Beam Interactions with Materials and Atoms*, 268(7-8), 736–738. Available from: https://doi.org/10.1016/j.nimb.2009.10.018

Yanites, B.J., Becker, J.K., Madritsch, H., Schnellmann, M. & Ehlers, T.A. (2017) Lithologic effects on landscape response to base level changes: a modeling study in the context of the Eastern Jura Mountains, Switzerland. *Journal of Geophysical Research: Earth Surface*, 122 (11), 2196–2222. Available from: https://doi.org/10.1002/2016JF004101.

Zondervan, J.R., Stokes, M., Boulton, S.J., Telfer, M.W. & Mather, A.E. (2020) Rock strength and structural controls on fluvial erodibility: implications for drainage divide mobility in a collisional mountain belt. *Earth and Planetary Science Letters*, 538, 116221. Available from: https://doi.org/10.1016/j.epsl.2020.116221

Zondervan, J.R., Whittaker, A.C., Bell, R.E., Watkins, S.E., Brooke, S.A.S. & Hann, M.G. (2020) New constraints on bedrock erodibility and landscape response times upstream of an active fault. *Geomorphology*, 351, 106937. Available from: https://doi.org/10.1016/J.GEOMORPH.2019.106937

SUPPORTING INFORMATION

Additional supporting information can be found online in the Supporting Information section at the end of this article.

How to cite this article: Boulton, S.J., Rodés, Á., Fabel, D., Alçiçek, M.C. & Whittaker, A.C. (2024) Complex erosional response to uplift and rock strength contrasts in transient river systems crossing an active normal fault revealed by ^{10}Be and ^{26}Al cosmogenic nuclide analyses. *Earth Surface Processes and Landforms*, 49(4), 1428–1450. Available from: https://doi.org/10.1002/esp.5778